eTransportation 12 (2022) 100167

Contents lists available at ScienceDirect

eTransportation

journal homepage: www.journals.elsevier.com/etransportation

Quantifying the state of the art of electric powertrains in battery electric vehicles: Range, efficiency, and lifetime from component to system level of the Volkswagen ID.3

Nikolaos Wassiliadis *, Matthias Steinsträter , Markus Schreiber , Philipp Rosner , Lorenzo Nicoletti , Florian Schmid , Manuel Ank , Olaf Teichert , Leo Wildfeuer , Jakob Schneider , Alexander Koch , Adrian König , Andreas Glatz , Josef Gandlgruber , Thomas Kröger , Xue Lin , Markus Lienkamp

Technical University of Munich (TUM), School of Engineering & Design, Department of Mobility Systems Engineering, Institute of Automotive Technology, Germany

ARTICLE INFO

Article history:
Received 24 December 2021
Received in revised form
15 March 2022
Accepted 9 April 2022
Available online 15 April 2022

Keywords:
Battery electric vehicles
State of the art
Teardown analysis
Electric powertrain efficiency
Lithium-ion battery
Battery aging

ABSTRACT

With the rise of battery electric vehicles to mass production, many technical improvements have been realized to drastically increase the electric range, efficiency, and sustainability. However, insights into those valuable state-of-the-art solutions are usually not shared with researchers due to the strict non-disclosure policies of electric vehicle manufacturers. Many studies, therefore, rely on assumptions, best-guess estimates, or insider knowledge. This article presents an in-depth multi-scale analysis of the electric powertrain characteristics of a Volkswagen ID.3 Pro Performance. The focus is set on the range, power, and lifetime perceivable by the user. Thorough experimental tests are performed from the battery cell to vehicle level, following the energy conversion from source to sink. Energy densities are determined at all levels and the absolute electric range is quantified under varying operating conditions. Power capability and efficiency is evaluated at cell level by quantifying the battery cell and pack performance with current rate tests in charge/discharge scenarios and impedance determination, as well as by determining powertrain energy conversion efficiency with in-vehicle measurements. Moreover, accelerated aging tests of the lithium-ion battery cells are performed with close to real-world conditions and projected to vehicle level, demonstrating that the lithium-ion battery pack achieves mileages outperforming the warranty information of the manufacturer under real-world operation. Overall, the results provide valuable insights into the current state of the art and can serve as a reference for automotive engineering in academia. Over 10 GB of lithium-ion battery cell, pack, and overall powertrain measurement data from the lab and real-world environment is available as open source alongside the article.

1. Introduction

The fast-paced environment of the transportation electrification, with electric vehicles reaching a share of 4.6% of global vehicle sales in 2020 [1], has led to major technological advancements in electric vehicles. The increased adoption of electric vehicles can be explained by the continuously improving range, efficiency, and lifetime of commercially available electric vehicles, which are achieved by international R&D efforts in academia and industry driven by political regulations to reduce particle emissions and the dependence on fossil fuels. Energy densities have increased up to two-fold over the last ten years and are expected to increase further [2], battery costs are rapidly declining, and battery electric vehicles (BEVs) are expected to reach TCO-price parity with combustion engine vehicles by 2025 at the latest [3].

In the recent decades, researchers have made substantial contributions to the improvements made in battery electric vehicle technology. In order to enable targeted research in academia at the edge of technology, knowledge and data on the state of the art of

* Corresponding author.
E-mail address: nikolaos.wassiliadis@tum.de (N. Wassiliadis).

https://doi.org/10.1016/j.etran.2022.100167

electric vehicles and their components is of utmost importance. However, electric vehicle manufacturers generally do not share the detailed specifications or measurement data of their products [4]. As a consequence, many studies addressing the design and operation of electric vehicles commonly rely on assumptions, best-guess estimates, and insider knowledge. For example, Harlow et al. [5] demonstrated that the battery cycle life and mileage in vehicle applications achieved by an optimized combination of state-of-the-art materials in lab-scale lithium-ion battery cells far exceed the lifetimes generally assumed for commercial batteries. However, as those cells are lab-scale cells, it is still not clear, how many cycles today's deployed industrial-scale automotive lithium-ion batteries achieve and how far or how long state-of-the-art battery electric vehicles travel with these lithium-ion battery packs.

Several studies have made information on electric vehicles available, both on the component and vehicle level. On the component level, a number of studies characterized the performance of different lithium-ion battery cells. For example, Barkholtz et al. [6] characterized four lithium-ion cells with a LCO, LFP, NCA, and NMC cathode, by determining the available discharge capacity at different temperatures and performing electrochemical impedance spectroscopy (EIS), and differential voltage analysis (DVA). However, the investigated cells were not representative of automotive-grade cells, as only commercially available 18650 cylindrical cells were tested. Muenzel et al. [7] investigated five cells with an LCO cathode from different manufacturers and performed capacity tests, detailed weight and dimension measurements, aging tests, EIS, and DVA. Furthermore, the authors provide a fully parameterized model of the investigated lithium-ion battery cell. However, only commercially available 18650 cylindrical cells were investigated here too. Bank et al. [8] characterized three high-power lithium-ion battery cells for 12 V/48 V vehicle applications, providing a full characterization of the investigated lithium-ion battery and parameter set for a battery model. However, the authors did not specify the vehicle models that the cells are used in. Momen et al. [9] presented the performance data and design details of the electric propulsion motor of the Chevrolet Bolt, including a measured motor efficiency map, but analysis of other powertrain components was outside the scope of this study.

Only a few studies quantify the status quo of electric powertrain performance at the vehicle level. Wegener et al. [10] disassembled an Audi Q5 hybrid battery system to determine the ability to feed lithium-ion battery packs into a second value-added cycle. The authors performed a case study on an ideal disassembly process and provided insights into the components of the overall battery pack. No additional properties of the battery pack were discussed. Kovachev et al. [11] disassembled and analyzed a battery pack of a commercially available BEV from a safety-related standpoint. Even though the authors did not specify the manufacturer, images reveal that the investigated battery pack had been extracted from a first-generation Nissan Leaf ZE0. Although many aspects have been shared with the scientific community, performance tests were not within the scope of the study. Recently, a similar study of a Nissan Leaf ZE0 module has been conducted by Marshall et al. [12], focusing on the recycling aspects of the battery's active materials. Besides the build-up of battery samples with recovered materials and the test of their functionality, none of the battery systems' performance parameters were revealed. Furthermore, both aforementioned studies rely on Nissan ZE0 series battery modules with a production date reaching back to the year 2010, which hampers a direct comparison to currently deployed battery packs in modern BEVs. Löbberding et al. [13] investigated energy densities of BEVs at multiple levels, however, stating that data from the investigated BEVs was aggregated from different references, such as online-available media, as comprehensive data is not available. Recently, Oh et al. [14] provided analysis to data of almost 383 vehicles including 27 BEVs. The data has been recorded via onboard in-vehicle measurements, which is why component data is limited to the battery pack current, voltage, SOC and engine rotations.

Although previous studies presented information on electric vehicles or their powertrain components, a joint investigation on both levels of state-of-the-art BEVs is not provided, most probably due to the required extensive effort of such studies. The Advanced Vehicle Testing and Evaluation study (AVTE) conducted in a collaborative effort of US national laboratories administrated by the National Energy Technology Laboratory (NETL) [15] is the only study that quantified vehicle performance both on a component and vehicle level. 30 different electric vehicles were tested between 2011 and 2018. Results at the vehicle level included battery pack capacity, charging efficiency, and energy consumption on various dynamometer test cycles and in various operating modes. At the component level, the tests included battery discharge tests, and monitoring of temperatures during battery cycling. Unfortunately, the results from this study do not represent the current state of the art anymore and are not enhanced with further analysis.

Based on this brief view on an extract of available studies at different scales and across different fields of research, it is apparent that little is known about what has already been achieved in electric vehicle design and operation on a system level. We believe that currently produced mass-series electric vehicles and, in particular, their energy storage systems are technologically far beyond the believed state of the art and that disclosure of quantified performance characteristics could prove the superiority of battery electric over combustion-powered vehicles and help independent researchers to identify and solve the remaining challenges in downstream studies.

1.1. Contributions

The underlying article presents an experimental investigation of the state-of-the-art electric powertrain of a Volkswagen ID.3 Pro Performance from cell to system level, to shed light onto the achievements and remaining challenges of BEVs. We performed an extensive characterization of the components following the energy conversion from source to sink and translated our findings to the impact on customer-relevant quantities such as range, efficiency, and lifetime. The main contributions of this study can be summarized as follows:

1. **Geometry, mass, and capacity determination for energy density calculations at multiple levels and experimental quantification of the electric range of the powertrain in different scenarios.**

The geometry and mass of the battery cell, module, and pack are measured and aligned with capacity measurements at battery cell and vehicle level to determine the gravimetric and volumetric energy density across the system integration path. The electric range is experimentally determined on a dynamometer using standardized international test procedures (e.g., WLTP and FTP-75) as well as real-world usage scenarios. The results are compared and analysis of the origin of deviations is provided.

2. **Quantification of the powertrain component power capability and efficiency in various vehicle conditions.**

The battery cell's resistance is characterized using current rate tests and impedance determination in the time and frequency-domain at various charge/discharge rates, the full state of charge (SOC) window, and a wide temperature range between 0 °C and 40 °C . At battery pack level, capacity and impedance scattering is

experimentally investigated and the thermal homogeneity of the battery module is recorded in real-world edge cases. Based on the results, the upper bound of the battery pack power capability is calculated for different usage situations. Moreover, the efficiency of the overall powertrain is evaluated in different real-world driving situations at vehicle level.

3. **Aging tests projected to vehicle level to yield an expected mileage and operating time of the battery pack.**

Real-world charge/discharge dynamics measured at the vehicle level are applied to battery cells in accelerated aging tests at a comparable lab environment to determine the cycle life of the battery cells in different usage scenarios. Based on recorded real-world usage data, the results are used to predict the mileage and the operating time of the BEV under study.

4. **Open access to extensive experimental data.**

Over 10 GB of measurement data recorded at different scales within this study (e.g., battery cell to pack geometries, battery currents, battery cell voltages, battery module temperatures, DC/DC power, electric machine torques and rotations, and many more) are published as open source alongside the article.

To the best of the authors' knowledge, this is the first article within the literature to present a broad multi-scale characterization, an in-depth performance assessment of an automotive state-of-the-art mass-series battery system, and its interplay with powertrain components at system level.

1.2. Layout

The article is structured as follows: Section 2 introduces the vehicle under study, the data acquisition technique, the teardown procedure of the battery system, the deployed experimental methods, and their boundary conditions. Subsequently, the three domains range, efficiency, and lifetime are addressed by analyzing and discussing the experimental results, as illustrated in Fig. 1. Section 3 compares the actual capacity of the cells to the accessible capacity during vehicle usage in relation to their mass and volume in order to determine the energy density at multiple levels. Also, the resulting absolute electric range in different scenarios is determined at vehicle level on a dynamometer and the causes for deviations are analyzed. In Section 4, current rate tests and impedance determination tests of the battery cell are performed. Based on the results, a lumped battery model is used to calculate the power capability of the energy storage and compare the energy conversion efficiency to the experimental results of the powertrain. Finally, in Section 5, battery aging tests are presented, and the overall mileage and operating time of the battery pack is estimated. Conclusions are drawn and an outlook is given in Section 6.

2. Vehicle under study, energy storage teardown and experimental techniques

At the beginning of this section, the vehicle under study and the data acquisition setup for the onboard electric powertrain measurements are presented. In the following, the teardown procedure of the battery and the final experimental setup for the cell-level tests are explained in more detail. Finally, all the experimental methods used and their boundary conditions are explained.

2.1. Vehicle under test and data acquisition

The Volkswagen ID.3 is a BEV available with storage systems of

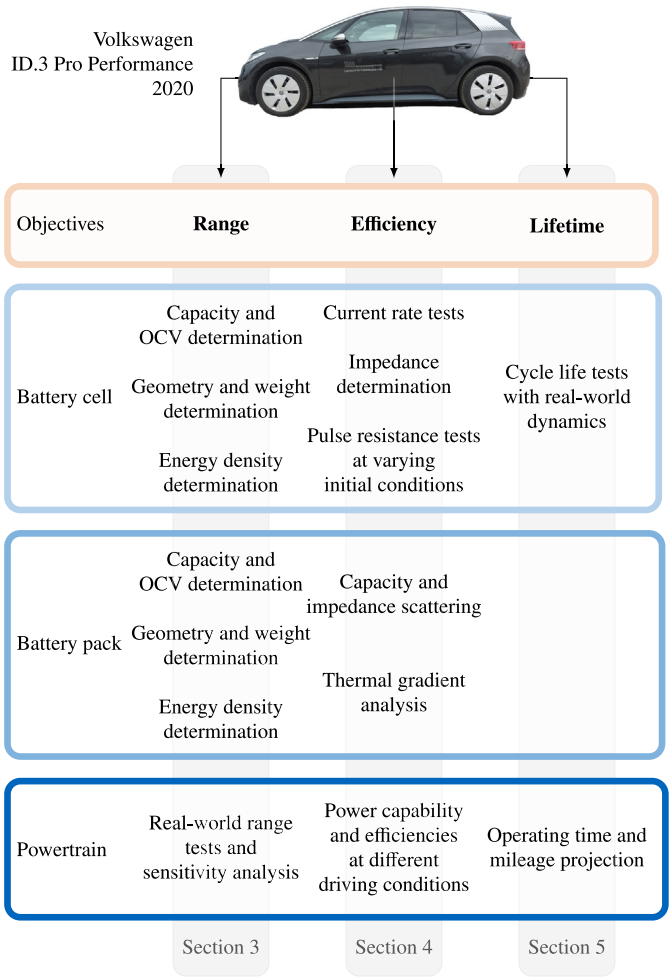

Fig. 1. The three domains range, efficiency, and lifetime of the underlying investigation in relation to the applied tests and methods to draw conclusions on the user-relevant objectives.

45 kWh, 58 kWh, and 77 kWh net energy content. In this study, an ID.3 Pro Performance from 2020 with the midsize battery pack (58 kWh) was acquired from a dealer to ensure we obtained an unmodified mass-series electric vehicle and to perform the vehicle level tests, as shown in Fig. 2(a). The vehicle under study has a measured mass of 1820 kg without loading, which is lower than the mass of 1891 kg stated by the manufacturer. It achieves an electric range of 408 km under the Worldwide Harmonized Light Vehicles Test Procedure (WLTP) according to the Certificate of Conformity (COC) of the vehicle [16]. The powertrain consists of a rear powertrain unit with a 70 kW continuous and 150 kW peak power synchronous motor. As seen in Fig. 2(b), the battery pack consists of nine separate battery modules contained in an underbody tray. A summary of the vehicle specifications can be found in Appendix A. During the study, the vehicle was operated on public roads, on a coast-down course, and on a vehicle dynamometer. To measure the vehicle's performance in dynamic conditions on the test bench, an automated throttle and brake control was designed and used.

In order to access the vehicle's onboard data during operation, a method similar to the method presented by Merkle et al. [17] was used. Data was recorded by regular querying of the component states via unified diagnostic services (UDS) over the OBD-II standardized interface of the vehicle. Relevant message identifiers (IDs) were assigned to the physical meaning of the signal by sniffing the

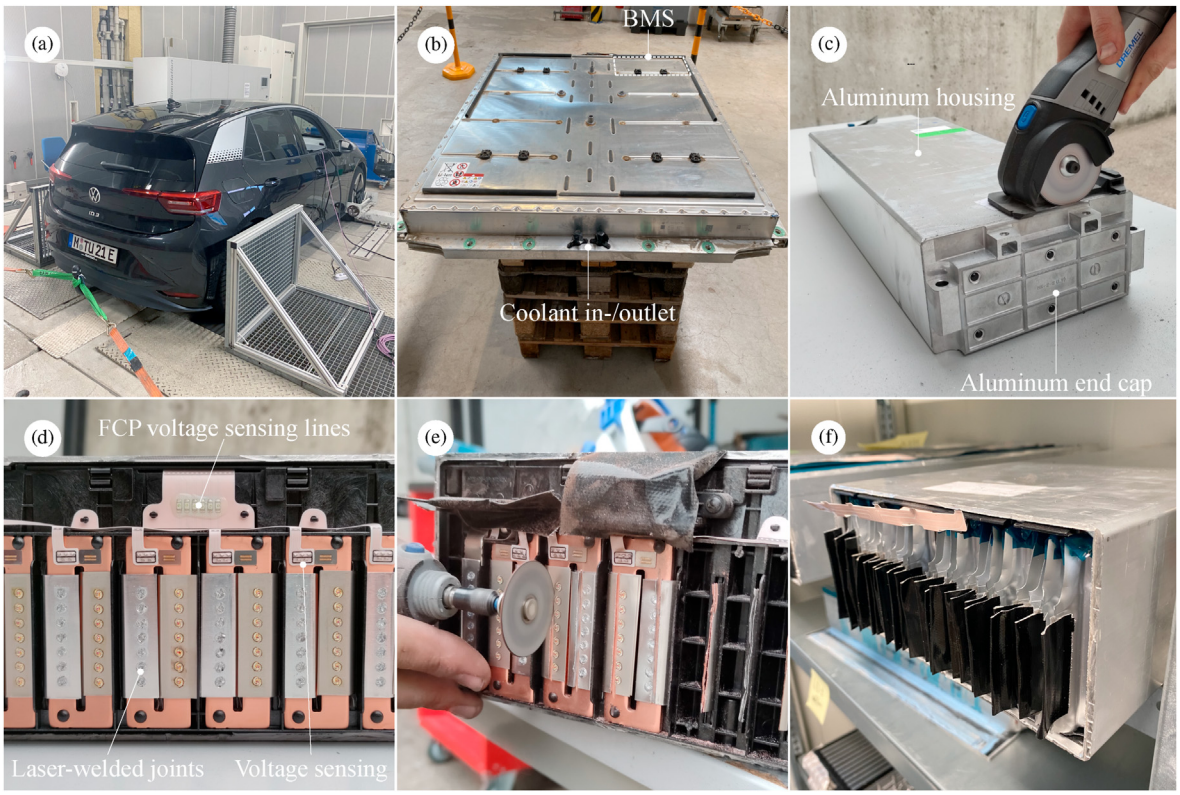

Fig. 2. Vehicle under test and tear-down procedure of the energy storage. (a) The experimental setup on the dynamometer. (b) The battery pack of the vehicle. (c)–(f) The battery module tray opening and the battery cell separation from the DC link.

controller area network (CAN) communication between the OBD-II interface and a commercially available workshop diagnostic tool. Prior to each data recording session, an extended diagnostic session was opened with a diagnostic session control request to enable full access to relevant control device messages. A summary of relevant IDs and their conversion to physical values for the underlying study is given in Appendix B.

2.2. Battery pack teardown

For further experimental assessment of the battery pack and the battery cells, three brand-new battery modules were acquired from a teardown vehicle (odometer reading less than 1000 km) and disassembled for experimental cell testing. It was ensured that the battery modules were similar to those mounted in the battery pack of the vehicle under study by a direct visual comparison. The disassembly procedure is illustrated in Fig. 2(c)–(f).

Each module has two 15 mm by 30 mm inter-module connection pads placed on the inward face (when assembled in the battery pack). An M6 threaded insert for bolting on the inter-module DC link is held in place by the module cap's plastic inner shell below the connection pad. The connection pads and outermost cell connection bus bars are manufactured as integral, stamped and bent stainless steel parts with a thickness of 4 mm and a width of 10 mm, only widening as they approach the connection pad. In between these cell-external connection bus bars, the individual cells are stacked to form a compact cell unit with all cells joined in parallel pairs, as seen in Fig. 2(d). The cell pairs in each module follow a zigzag path along the module and are connected in series, resulting in a 12s2p configuration. Excluding the already mentioned external connection bus bars, this layout requires five internal bus bars on the inward side (where the external connections are placed) and six on the opposing one. All of these are stamped, rectangular (70 mm by 23.6 mm) 3 mm thick copper parts with rectangular (51.5 mm by 3.5 mm) cutouts in the middle to allow for cell electrode tabs to be fed through and two holes for fastening to a polymer bracket separating the bus bars from each other. The internal bus bars directly neighboring the external connection pad bars feature an additional small cutout in the upper outside corner for voltage sensing lines, as visible in Fig. 2(e). Each internal bus bar is equipped with a double laser line welded pad for connecting the flexible printed circuit (FPC) style voltage sensing cable by a five-point piercing action. These are routed via resistors towards a connector on the inward module face, where they join the connections for the two temperature sensors (four-wire resistive type) located on top of the cell stack. There are no further battery management system (BMS) components incorporated in the module. The two 45 mm wide and 0.4 mm thick aluminum cathode tabs from each cell pair are stacked and joined onto one side of the internal bus bar with seven spot welds, as are the two 45 mm wide and 0.2 mm thick nickel-plated copper anode tabs from the next pair on the other side of the cutout. Both the cathode and anode tabs are laser-welded in a two-line spiral fashion, but resulting in visually different appearances of the aluminum-copper and nickel/copper-copper welds. The same technique is used to join the first and last cell pair's tabs to the external connection bus bars, respectively. During module assembly, the cells are inserted into a rectangular and tubular aluminum housing together with a polymer cover on top containing the temperature sensors, onto which the two polymer brackets holding the bus bars are placed as seen in Fig. 2(f), and enclosed by welding on aluminum end caps. The cell stack incorporates a foamed polymer spacer inbetween cell pairs 6 and 7 enabling cell extension, e. g. in cycling. Whether it is used to precompress the cell stack is unknown. There is no further clamping device around the cell stack. Thermally conductive resin is then injected through holes on the underside of the tubular

housing to connect the individual cells to the battery pack's floor-mounted thermal management system.

2.3. Battery cell under test

The battery module, that was opened on both end faces, was then used for electrical cell tests. In order to achieve reliable results, it is important to sustain similar conditions to the conditions present in the battery system, as e.g., compression pressure highly affects the cycle life of the pouch cells [18] or the electrical contact resistance may interfere with the thermal behavior of the cell [19]. Even though many studies apply a specific compression pressure onto pouch cells, it is usually not clear how they will be stressed in the target application. We, therefore, kept the investigated pouch cells within the housing during testing by carefully disassembling the two lids of the battery module and removing the external cell connection to the DC bus bar. The exposed contacts of all cells can be connected to a measuring device but are still contained within the surrounding casing, which ensures a compression pressure similar to the in-vehicle scenario.

Experiments were performed by connecting the battery cell to an *MRS-6V* battery cycler (BaSyTec GmbH, Germany) with a maximum current of ±600 A and a current and voltage accuracy of ±300 mA/±0.3 mV, except where noted otherwise. A copper clamping contact was designed to yield a good contact to the pouch tabs of a single cell. The mechanism can be shifted in the lateral direction to contact a specific battery cell of all 24 cells within the battery module. For safety reasons, the cell temperature was monitored by two thermal couples at the top of the cells close to the tab positions. Note that although this setup enables the measurement of realistic cycling behavior, critical temperature evolution is only present at the respective single cell during cycling, which allows for undesired heat compensation through the surrounding cells. The battery system was placed into a *VC*^{3} *4100* thermal chamber (Vötsch GmbH, Germany) and was conditioned at the given temperature for characterization and cycling. The overall setup is illustrated in Fig. 3 including an image of the single-cell copper clamping contact.

2.4. Experimental techniques

In the following subsections, the methods and boundary conditions applied in this study are specified from cell to system level.

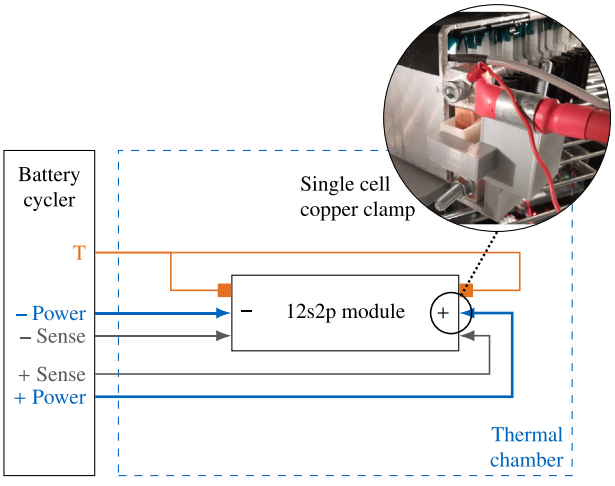

Fig. 3. Setup for single cell measurements of the battery cell under a predefined, real-world preload within the battery module. The battery cycling equipment is connected directly to the cell tabs, which have been carefully exposed from the bus bar.

2.4.1. Capacity and open-circuit voltage determination

To determine the cell capacity and open circuit voltage (OCV), both constant current (CC) charge and discharge procedures are applied to a single cell within the opened module at currents of C/50 (1.56 A), C/40 (1.95 A) and C/10 (7.8 A), between voltage bounds of 2.5 and 4.2 V and at 20 °C ambient temperature. As the applied currents are comparatively low to the currents in real-world operation and the required current precision is high, a *CTS* battery cycler (BaSyTec GmbH, Germany) with a current and voltage accuracy of ±0.2 µA/±1 mV has been used for the C/50 and C/40 measurement. For the remaining measurements, a *XCTS25* battery cycler (BaSyTec GmbH, Germany) with a current and voltage accuracy of ±50 mA/±3 mV has been used. This procedure is well-known as the pseudo-open circuit voltage (pOCV) technique in the literature [20].

For a direct comparison to the vehicle level, the storage system is completely discharged by driving to 0% SOC displayed in the user interface (UI) and subsequently using of the cabin heater until the control logic automatically shuts off the current and vehicle. Afterwards, the vehicle is charged with the lowest selectable power of 1.2 kW, resulting in a close match to a C/40 charging current at cell level. The test has been conducted at 20 °C ambient temperature. Since such a procedure is not feasible for the discharge direction, the charge direction is selected as the SOC reference for comparability. The voltage and current response of the entire battery system is used for this procedure to ensure robust results as the parameter scattering of 216 cells superimposes and averages out. This approach, however, dilutes the distinctiveness of features visible in single cell measurements.

2.4.2. Battery cell current rate tests

In addition, current rate tests of a single cell were performed with C/10 to 3 C constant current constant voltage (CCCV) charge and discharge protocols between 2.5 and 4.2 V and a cut-off current of C/20 in charge and discharge direction. Between each charge or discharge cycle, a thermal relaxation of 2 h was ensured. The testing procedure was performed at 20 °C ambient temperature.

2.4.3. Battery cell resistance tests

To quantify the efficiency and power capability of the cell, the DC resistance was determined at a wide operating range. Therefore, a test procedure consisting of 30 s current pulses with different C-Rates (±0.5C, ±1C, and ±2C) was performed at each 10% SOC between 10% SOC and 90% SOC and at 0 °C, 20 °C, and 40 °C. The time resolution of the measurement device is 1 µs and the sampling interval was set to 20 ms with an additional first sample point after 1 ms. The DC resistance after a specific time step t was then calculated by using Ohm's law according to $R_{DC,t} = (U_t - U_0)/I$ with the voltage U_0 right before the current pulse and the current magnitude I. To cover a wide range of dynamics, which can occur during the vehicle usage and charging, $R_{DC,t}$ was evaluated at 1 ms, 100 ms, 1 s, 10 s, and 30 s.

2.4.4. Battery module capacity and impedance scattering tests

The capacities and impedances were experimentally determined for all cells in the battery module. Capacities were quantified by an initial CCCV charge and a consecutive C/3 CCCV discharge with a cut-off current of C/20. After the capacity determination, all cells were directly charged to 50% SOC and relaxed for more than 4 h to reach an equilibrium state. Subsequently, EIS measurements were conducted. All EIS measurements were performed with an *Interface 5000E* potentiostat (Gamry Instruments Inc., USA), using the hybrid EIS mode with an AC RMS voltage of 4 mV and a frequency range from 5 kHz to 10 mHz with ten points per decade. All tests were performed at 20 °C ± 0.2 °C ambient temperature.

2.4.5. Battery cycle life and reference performance tests

Three cells from the battery module were subjected to an accelerated aging test with cell-specific charge/discharge dynamics, using the test setup illustrated in Fig. 3. For the sake of readability, the discharge sequences are introduced later in Subsection 5.1. In order to avoid thermal interactions, two non-adjacent cells within the module were chosen for the aging tests and connected to the battery tester. The rest of the module was at rest. The above-mentioned aging acceleration was achieved by skipping the idle times between the charge/discharge sequences in order to shorten the test duration. However, to not manipulate the actual load profiles and thus to ensure the replication of the real aging effects, we do not modify the stress factors of the cycles. Referring to Epding et al. [21], the omission of intermediate rest periods leads to a more conservative aging prediction since those periods trigger reversible capacity recovery and therefore slow down the genuine aging process. Every 50th cycle as well as before starting the test, a reference performance test (RPT) was conducted to characterize the cell under normalized conditions. Between the end of the 50th cycle and the beginning of the RPT the cells are at rest for 15 min. Afterwards, the cells are fully charged by means of C/3 CCCV followed by another 15 min of idle time before measuring the capacity. The RPT consists of a consecutive C/3 CCCV discharge/charge sequence, a C/15 discharge/charge sequence between 2.5 V and 4.2 V and a high pulse power characterization procedure at various SOC. All cells in the cycle life test were subjected to this procedure. All tests were performed at 20 °C ambient temperature. Note that an active cooling system, such as the Volkswagen battery pack bottom cooling plate as in the pristine battery pack, was not deployed.

2.4.6. Vehicle coast-down procedure and driving resistance determination

The vehicle was subjected to coast-down tests to determine the driving resistances for an accurate simulation of the vehicle under transient load on the dynamometer. The coast-down tests were performed at a 1.5 km long flat track on a calm day with a constant wind velocity of less than 2 m/s. To minimize external influence due to, e.g., small height differences, we performed two coast-downs in both track directions and averaged the results. The overall procedure was performed for five velocity intervals, i.e., 0–40, 40–60, 60–90, 90–115, and 115–135 km/h, to account for the limited track distance. Prior to the coast-down procedures, the vehicle was weighed and preconditioned by 20 min of dynamic driving to replicate friction losses in real-driving conditions. The achieved velocity profile was then used to calibrate the driving resistance equation

$$F = ma = \underbrace{mgf_{\mathrm{RR}}}_{\text{Rolling resistance}} + \underbrace{0.5\rho v^2 c_{\mathrm{d}} A}_{\text{Aerodynamic resistance}} + \underbrace{(m+\lambda)a}_{\text{Inertia}} \tag{1}$$

with the vehicle mass m, gravitational acceleration g, rolling resistance coefficient f_{RR}, air density ρ, velocity v, aerodynamic resistance coefficient c_{d}, frontal vehicle surface A, and the mass equivalent inertia λ. To account for the resistances proportional to v and v^2, a polynomial regression using the base function

$$F_{\mathrm{fit}} = a_0 + a_1 v + a_2 v^2 \tag{2}$$

yields $a_0 = 121.7\ N$, $a_1 = 4.62\ N/(m/s)$, and $a_2 = 0.275\ N/(m/s)^2$ as the most accurate parameters with an RMSE of 0.76 km/h. For further information on the experimental results and the calibration procedure, the reader is referred to Appendix C.

2.4.7. Vehicle dynamometer and charging tests

The vehicle was subjected to discharge tests with a single-axis 250 kW dynamometer (Renk GmbH, Germany). The tests performed can be divided into three test series.

The first test series on the vehicle dynamometer served to determine the range in standardized international test procedures and real-world usage situations. Routes in public road traffic were driven to represent an urban (8.1 km), interurban (20.1 km), and highway (35.2 km) scenario. The recorded velocity profiles were repeated on the chassis dynamometer using an automated throttle and brake control. To determine the absolute electric range, the cycles were run until the vehicle could no longer follow the target velocity. Each real-world driving cycle was measured at 15 °C and 30 °C ambient temperature with the heating, ventilation and air conditioning (HVAC) of the cabin inactive to investigate a possible impact of component temperatures or cooling on the energy consumption. Following the same procedure, the WLTP and FTP-75 cycle were run repeatedly at an ambient temperature of 23 °C, which is a requirement of the test procedure specification. The three real-world cycles were driven at a similiar ambient temperature of 23 °C and a starting SOC of 80% to compare it to the international test procedures and measure the battery currents and voltages for transferring the results to the battery laboratory. Fig. 4 shows the velocity profile and the measured battery current and voltage as well as the frequency of the C-Rate with a starting SOC of 80% in each case. The urban cycle is less dynamic and therefore the battery is only slightly discharged with an average of 0.09 C and a maximum of 0.7 C respectively. While 1.3 kWh of traction energy was measured in the urban cycle, 8.5 kWh was measured in the highway cycle. In addition, a higher proportion of large discharge C-Rates can be observed, which is also reflected in the ratio of recovered to total energy. For example, 31% is recovered in the city cycle, while only 16% is recovered in the highway cycle.

Within the second test series, the electric range at constant speeds was examined. Likewise to the previous test series, an automated throttle and brake control was used to maintain a constant velocity. The range at the different speeds was calculated from the energy consumption at the operating point and the useable battery capacity. To account for external influences, the tests were performed at 15 °C and 30 °C ambient temperature. In addition, each measurement was performed in the high ($>70\,\%$) and low ($<30\,\%$) SOC range to hedge against varying efficiencies of different DC link voltages.

The third test series investigated the efficiency of the electric motor and inverter. The chassis dynamometer was set to speed control. With an accelerator pedal control, different load points (speed and torque combinations) were kept static, and each operating point was held for 15 s. The minimal controllable speed and torque were 4 km/h and 16 N m, respectively. Measurements were performed at an ambient temperature of 23 °C. It should be noted, that the DC link voltage should be kept static at all measurement points to avoid different operating points of the inverter. However, this is not possible by nature of the experimental setup, as the control devices prevent the operation of the vehicle with an artificial DC source. To keep the conditions as constant as possible, we operated the vehicle in an SOC range of 30%–70% to minimize the DC link voltage differences. It should be noted, however, that the resulting characteristic map may suffer under a certain amount of deterioration compared to the experimental assessment of the powertrain unit itself.

In addition, vehicle charging tests were performed. The vehicle was charged between 0% and 100% SOC displayed in the user interface (UI) using an 11 kW AC wallbox leading to a constant power (CP) charging protocol. Note that the UI-SOC inherits capacity reserve margins and is typically above the actual battery cell

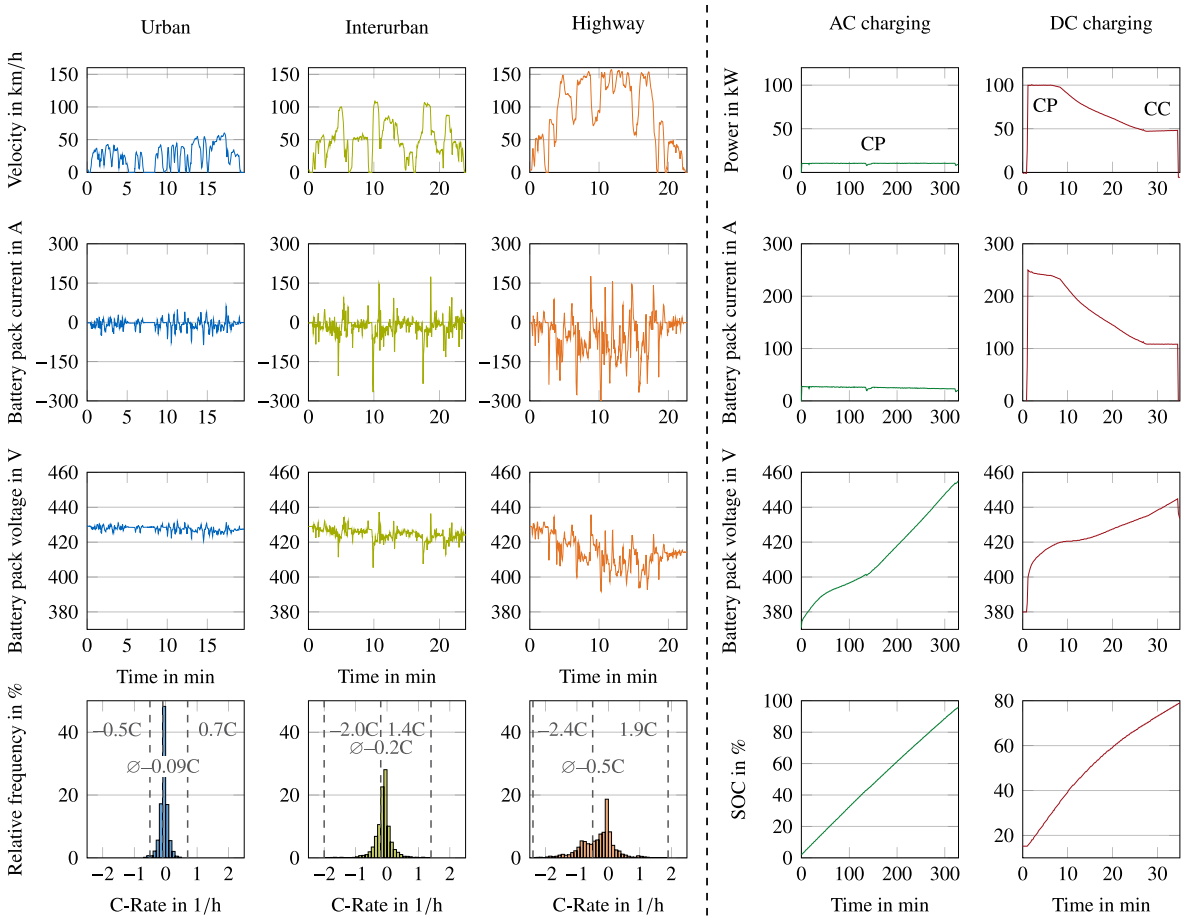

Fig. 4. Three real-world usage patterns measured during vehicle operation. Measured vehicle velocity, pack current, voltage, and load spectrum analysis for the urban, interurban, and highway driving scenario. Discharge sequences measured from 80% UI-SOC. Note that grey dashed lines illustrate the minima, maxima and arithmetic average of the underlying event. Measured pack power, current and voltage for an 11 kW AC charge and 11 kW DC fast charge event. AC charging between 0 and 100% UI-SOC. DC fast charging between 10 and 80% UI-SOC. Note that the illustrated SOC represents the actual SOC of the battery pack.

or pack SOC. No constant voltage (CV) sequence had been observed at the end of the AC charging event. DC fast charging was performed between 10% and 80% UI-SOC. To do so, the vehicle was previously discharged by driving on a highway starting from 100% UI-SOC to thermally precondition the battery pack. The actual starting SOC of the battery pack was 16% SOC. During the DC fast charging procedure, a 100 kW CP protocol up to an actual SOC of ~35% and a subsequently reduced fast charging current was observed. From ~70% actual SOC, charging is continued with a CC current of 110 A. Again, no constant voltage phase was observed until the manually aborted end of charging at an actual SOC of ~78%.

3. Range

The electric range of a BEV is primarily determined by the battery system. As energy density is a crucial parameter for its performance, we pose the following question: *How large are energy density losses along the system integration path of the battery pack?* To answer it, we investigated the battery pack system at the cell, module, and pack level to gain insights into their range-related properties. Additionally, powertrain tests were performed at vehicle level by applying different use-case situations to answer the overarching question: *How far can state-of-the-art BEVs travel in realistic use-case situations?*

3.1. Battery cell level considerations

The battery cells each measure 545 mm (excluding tabs) by 98 mm by 8.65 mm as shown in Fig. 5(a), displace 0.438 L and have a mass of 1.101 kg. Fig. 6(a) shows the measured pOCV for the C/40 vehicle level procedure from subsection 2.4.1 (which is only possible in the charging direction using the onboard charger at minimum power) as well as the comparable cell level tests. In the former, an average of 74.76 Ah and 280.6 Wh are charged per cell. The minimum and maximum detected cell pair voltages were 3.25 V and 4.19 V, respectively, indicating some cell-to-cell OCV variation when comparing to the average values of 3.328 V and 4.185 V.

Individual cell charging at C/40 between extended bounds of 2.5 V and 4.2 V yielded a larger capacity of 80.45 Ah and 300.3 Wh, which are taken as the cell's reference values from here on. The resulting gravimetric and volumetric energy densities compute as 273 Wh/kg and 685 Wh/L, respectively, which are very similar values to ones identified in literature analyzing an identical cell [22]. As a reference, the Jaguar I-Pace has been reported to achieve a gravimetric and volumetric energy densities of 257 Wh/kg and 541 Wh/L at cell level [23], which are respectively 4% and 19% lower than the ones identified for the ID.3, confirming an efficient integration in the latter. Comparing to the vehicle level test, about 4% of the total cell energy content in the low SOC range and 3% in the high SOC range are made inaccessible to the driver by the vehicle

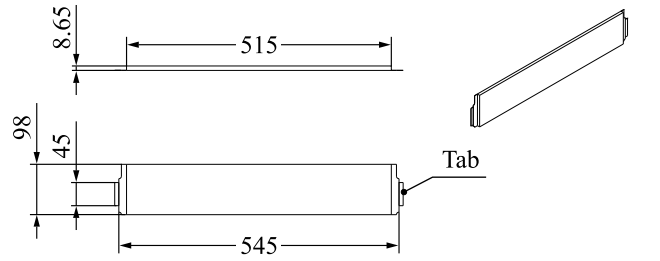

(a) Battery cell dimensions

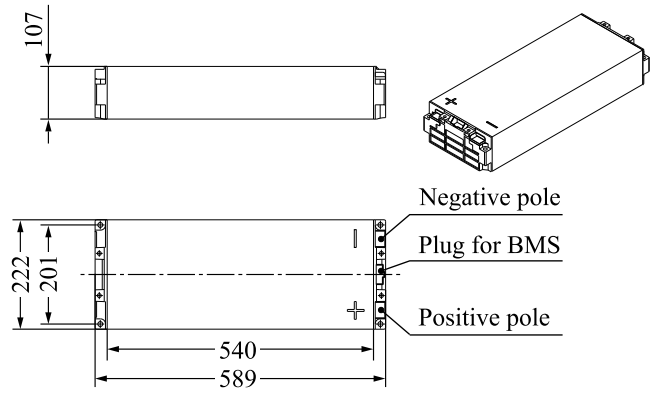

(b) Battery module dimensions

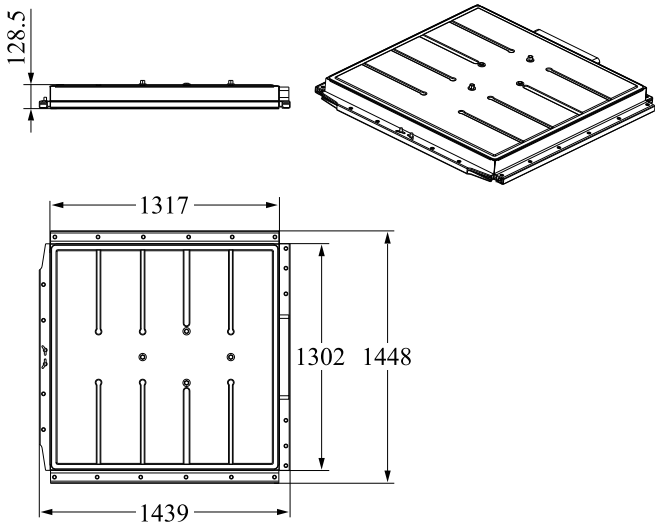

(c) Battery pack dimensions

Fig. 5. Overview of the main geometrical measures of the battery cell, module, and pack. All values are in mm. Note that the drawings are not true to scale. For further geometrical analysis, the reader is referred to the reconstructed geometrical models provided along with the article.

software by restricting the cycling range. Discharging under otherwise equal conditions, the cell delivered 79.48 Ah and 293.7 Wh. Comparing the charge and discharge directions, the coulombic and energy efficiencies in the cycle are 98.7% and 97.8%, respectively.

DVA is a common tool for identifying characteristic stage transitions of the electrodes' materials and gaining insights into their properties [25,26]. In this work, the pOCV cycles' measured voltage and current values from the are smoothed out using a simple unweighted moving mean algorithm to reduce signal noise employing a window length of 5 s and 40 s, respectively. The normalized differential voltage U_{DVA} is calculated using

$$U_{\mathrm{DVA}} = Q_0\left|\frac{dU}{dQ}\right| = Q_0\left|\frac{dU}{dt}\,\frac{dt}{dQ}\right| = Q_0\left|\frac{dU}{I\,dt}\right| \approx Q_0\left|\frac{\Delta U}{I\Delta t}\right| \tag{3}$$

for each timestamp transition. Fig. 6(b) shows the normalized DVA from all three C/40 pOCV procedures and a characteristic NMC 811/SiC curve recorded at C/30 on an LG Chem INR18650MJ1 full cell [24] for comparison. For enhanced readability and comparability, only absolute values are used for both charge and discharge directions. Q_0 is the single cell reference capacity. To verify the measurements, other C-Rates and methods were also used to determine the OCV and are detailed in Appendix D.

Starting with the cathode, recent studies reported $\mathrm{Li[Ni_{0.65}Co_{0.2}Mn_{0.15}]O_2}$ (colloquially called NMC 712) as the cathode active material [22], while the vehicle manufacturer laid out NMC 622 and NMC 811 as development steps earlier [27]. A higher nickel content enables a higher active material charge and therefore energy density [28]. Jung et al. [29] identified characteristic differences in DVA (more precisely in its inverse, the incremental capacity analysis) between NMC 811, exhibiting two notable phase transition features at 3.95 V–4.15 V vs. $\mathrm{Li/Li^+}$ in a half-cell setup, and NMC 622, where both appear less pronounced and at higher electrode potentials. As only the lower potential range of NMC 811 is safely reachable in a full cell setup, this material should be identifiable via DVA thanks to the straight superposition of electrode effects. Noh et al. [30] found similar indicators for NMC 811, but only registered them to a much lower extent in a $\mathrm{Li[Ni_{0.7}Co_{0.15}Mn_{0.15}]O_2}$ cathode composition similar to the discussed NMC 712 material.

The measured discharge curve features a prominent increase in differential voltage over the charge curve close to 100% SOC due to the test plan not incorporating sufficient relaxation before the pOCV discharge and therefore superimposing the relaxation of remaining charge overpotentials and thermodynamic cell discharge behavior. Notably, however, a distinct deep minimum as expected from literature and shown by Sturm et al. [24] in a full cell NMC 811 setup around 90% SOC is missing, indicating a nickel content of below 80%.

For the anode, silicon is increasingly being formulated into commercial cells' graphite active material to enhance energy density at the risk of more harmful cycling due to silicon's high volume expansion during cycling, *inter alia* [31]. Zilberman et al. [32] found SiC anodes exhibit a less pronounced increase in potential towards complete delithiation than pure graphite with their investigated cell having a silicon mass content of 3.5% [24]. This results in multiple characteristic features such as a plateau in the full cell DVA at 0%–15% SOC encoding information on the silicon's capacity. The four characteristic maxima at around 20% and 60% SOC indicate the (dis)appearance of graphite-lithium intercalation stages and their relative position in the spectrum can therefore serve as an indicator of trends in anode storage capacity and cell balancing [33]. In our measurement, all four graphite-induced maxima are visible. Crucially, however, no discernible silicon features towards anode delithiation are present, which is on par with a recent material study of the cell [22]. Larger shares of silicon could be therefore used to further increase the energy density and therefore the overall electric range of the vehicle.

The dashed vehicle level DVA shows the same tendencies as the single-cell measurement, indicating the former's validity, but does not provide as much detail in individual peaks due to the superposition of the multiple cells' individual features. It does, however, provide enough detail to possibly track aging phenomena through peak shifts in slow charging cycles over time, which might become a valuable diagnostic tool at the vehicle level.

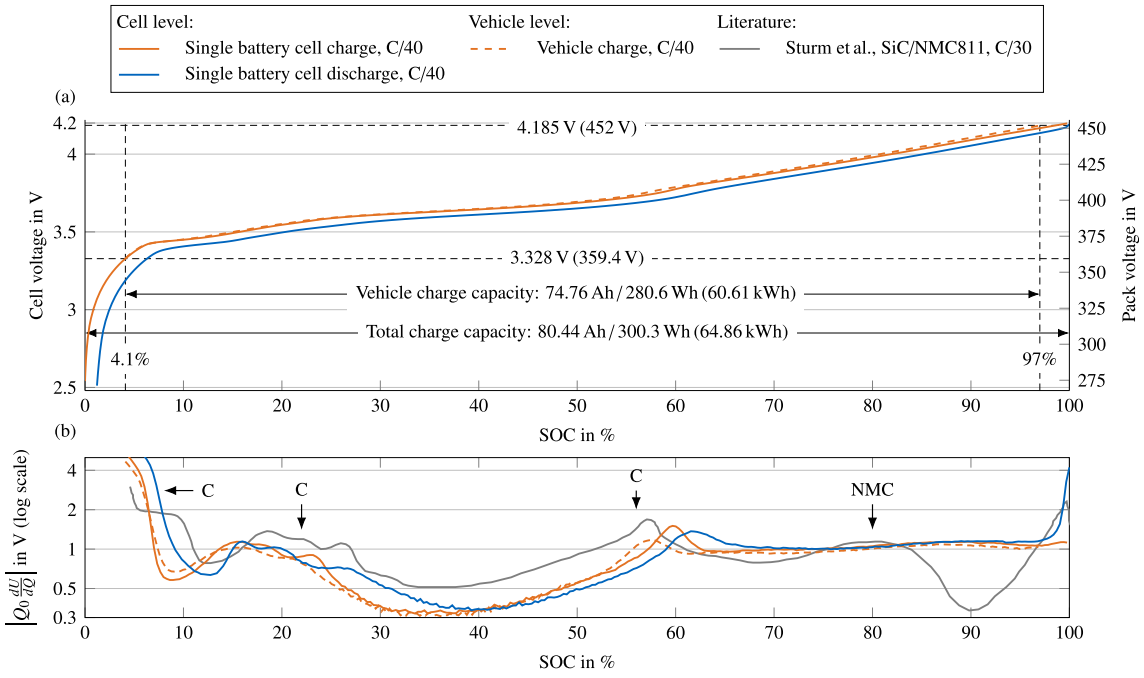

Fig. 6. Open-circuit voltage (OCV) of the battery taken from a C/40 single cell and vehicle level measurement. (a) OCV curves indicating charge and energy throughput as well the useable capacity in the vehicle. (b) Corresponding DVA curves showing no features of exceptionally high nickel or silicon content in comparison to literature values for a NMC 811/SiC cell [24]. (For interpretation of the references to colour in this figure legend, the reader is referred to the Web version of this article.)

3.2. Battery module level considerations

As shown in Fig. 5(b), an individual module measures 589 mm by 222 mm by 107 mm, displaces 13.6 L (derived from CAD), and has a mass of 30.9 kg. Each module contains 24 cells in a 12s2p configuration and stores 7.2 kWh when projected from the cell's reference energy content accordingly. The gravimetric and volumetric energy densities compute to 233 Wh/kg and 530 Wh/L, respectively. The module voltage is in the range of 30 V–50.4 V, of which only 39.9 V–50.2 V are allowed on the vehicle level. The upper voltage limit falls below the IEC60449 extra-low voltage threshold of 60 V without touch protection and therefore requires fewer safety precautions. A comparison between the module, and cell reveals that 23% of the module's volume and 15% of the module's mass is comprised of non-cell material (e.g., housing, heat-conducting paste, spacers, cell connections, battery management sensors, and cabling), leading to equivalent losses in energy density. Fig. 7 illustrates these losses in volumetric and gravimetric energy densities from cell to module and pack level.

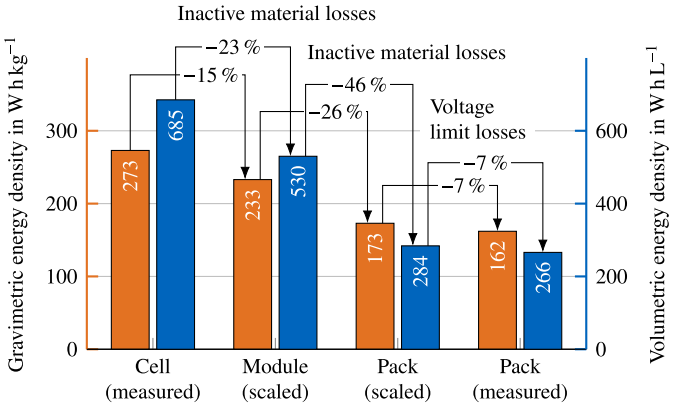

Fig. 7. Energy densities experimentally determined with C/40 CC charge sequences, weighing and geometrical measurements at multiple integration levels. For further details on the actual measured and scaled values, see Appendix E.

3.3. Battery pack level considerations

For the investigated midrange 58 kWh battery pack variant, nine modules are arranged in two rows parallel to the vehicle's longitudinal axis. The remaining space in the rear of the left hand side row is used to install the BMS and further electrical components. For comparison, the 45 kWh variant uses seven modules in a similar arrangement with shorter rows, while the 77 kWh variant uses twelve modules in a symmetrical arrangement with the BMS located behind all modules. The battery pack housing is scaled accordingly and for the two smaller variants, the remaining space on the underside of the vehicle is covered with a stiffening plate. The investigated battery pack measures 1439 mm by 1448 mm by 128.5 mm in total (including the battery sills), displaces 228.2 L (derived from CAD), and weighs 375 kg including the liquid coolant contained in its coolant channels on the bottom side. The theoretical energy content from the cell's reference energy content scales up to 64.9 kWh in the overall 9s(12s2p) configuration resulting in pack level gravimetric and volumetric energy densities of 173 Wh/kg and 284 Wh/L, respectively. However, only 59.3 kWh of the energy content are accessible to the driver due to the aforementioned cycling range limitations, which is still more than the nominal value of 58 kWh given by the manufacturer. For comparison, the Audi e-tron has energy densities of 136 Wh/kg and 216 Wh/L at pack level [34] which are 21% and 24% lower than the respective values of the investigated Volkswagen ID.3 pack. Comparing module to pack values of the Volkswagen ID.3, a non-module mass of 96.7 kg, making up 26% of the entire pack mass, resulting in an equally large gravimetric density loss, and a non-module volume share (and volumetric density loss) of 46% become apparent, as shown in Fig. 7. These masses and spaces are comprised of the battery pack housing, internal structural and

cooling elements, inter-module DC links, fasteners, electrical connectors, and BMS equipment (e.g., control unit, cabling, sensors, relays, and emergency disconnectors). Further details on the energy density calculations can be found in Appendix E.

Fig. 7 shows the energy densities when taking the vehicle level test procedure from Section 2.4.1 as a basis for the energy content in the rightmost columns. These show the effect of the cycling range limitation imposed by the BMS which reduces the useable cell voltage, thus causing an energy density drop at the pack level. As discussed in Section 3.1, the measured cell voltages in the vehicle level test cover a range of 3.25 V–4.19 V. Extending the useable cell energy range by reducing the cell voltage spread and overpotentials relevant in higher current situation than tested here increases the useable pack energy and thus raises the vehicle range. If the lower cell voltage limit could be shifted from 3.25 V to 2.5 V this would lead to a pack level energy gain of only 2.21 kWh assuming cell voltage spread as measured on vehicle level and full exploitability of the extra charge. An extension of the upper cell voltage limit to 4.2 V would yield even lower gains at 0.96 kWh. Assuming a constant vehicle consumption of 15.4 kWh/100km, this bound shifting would result in a slight range increase of 14 km (3.3%) and 6 km (1.2%), respectively. However, this voltage range extension is probably avoided as it may cause accelerated aging while the range gain is small.

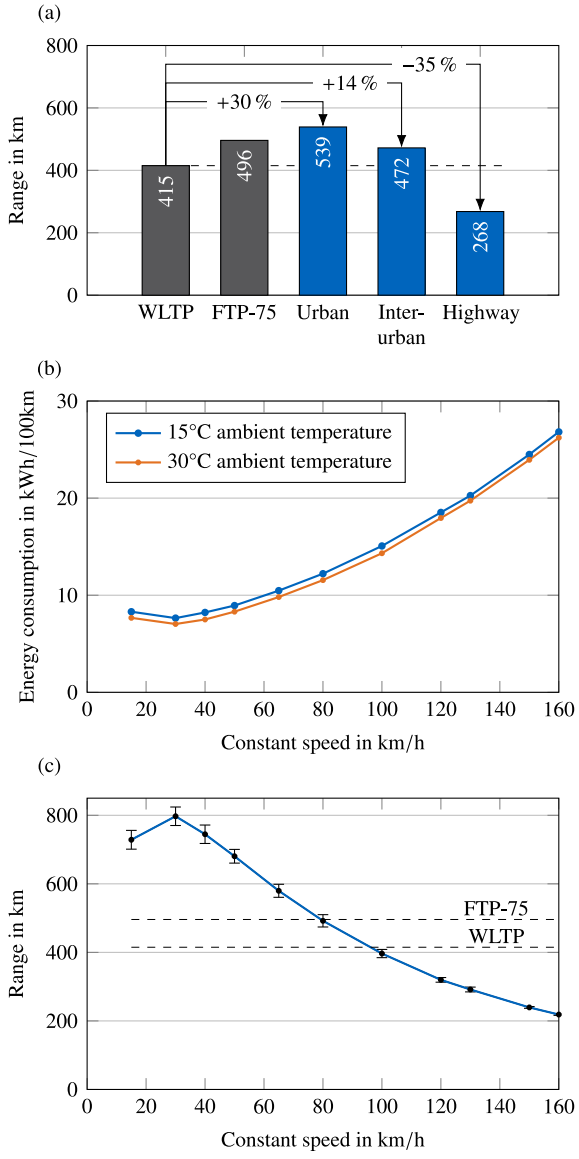

Fig. 8. Experimentally determined travel distances. (a) Maximum achievable range in international test procedures compared to real-world cycles. (b) Experimentally determined energy consumption at constant speeds. (c) Maximum achievable range at constant speeds. Note that all experiments in (a) have been performed by continuously driving of the vehicle until it could not follow the target velocity anymore. Energy consumption in (b) is measured at discrete intervals and extrapolated with the extractable energy in the WLTP scenario, gaining the maximum achievable range of the vehicle, visualized in (c).

3.4. Real-world range and influencing factors

Fig. 8(a) shows the absolute ranges of the driving cycles measured on the dynamometer according to Section 2.4.7. Here, the vehicle achieved an absolute range of 415 km under the WLTP sequence, which is close to the manufacturer's specifications of 408 km. This corresponds to a deviation of 1.7% from the official specifications, which is tolerable considering the complexity of the measurement task and confirms the validity of the dynamometer test. The cause of the deviations may be the driving resistance parameters, which were determined on the basis of the coast-down tests. The WLTP range is exceeded by the range of the urban cycle by up to 30% due to its lower speed and the associated lower energy consumption. Even in the interurban cycle, an increased range of 14% was measured. The absolute range achieved in the highway cycle of 268 km drops by 35% compared to the WLTP range due to the high power consumption at high speeds.

The ranges at constant speed levels are shown in Fig. 8(b). When the ambient temperature or SOC-level was varied, only a small influence on consumption and thus range could be determined. In general, high ambient temperatures are more beneficially due to lower losses, while low SOC-level also decrease the energy consumption. As a reference to the reader, the measured deviations are shown in Fig. 8(b) as error bars above the mean value. It should be noted, that the HVAC was switched off in all scenarios to allow for comparability of the results. The maximum range of 797 km can be achieved at a constant speed of 30 km/h as drag losses are low. At the vehicle's maximum speed of 160 km/h, the achievable absolute range reduces to 218 km. In brief, the specified WLTP range achieves a closer estimate on the achievable range in real-world highway scenarios than the specified FTP-75 range, while the urban and interurban scenarios are better represented by the FTP-75 range specification. Large differences between the different scenarios occur, which may be traced back to inefficiencies or the varying power capability of the vehicle, which is therefore assessed in the following section.

4. Efficiency

A high electric efficiency of the electric powertrain avoids oversizing the electric powertrain and thermal management, ensures efficient use of resources, and keeps the costs low. If the cell resistances are high, voltage bounds are rapidly reached and limit power delivery as the battery cell voltages may exceed operating boundaries. Furthermore, thermal losses are amplified as they are directly proportional to the resistance and lower voltages lead to a higher current at a given power requirement. Current rate tests with a single cell were performed to yield insights into the efficiency and power capability of the state-of-the-art lithium-ion battery under study. As the weakest parallel-connected cell pair in the battery pack defines the system power capability, the capacity and resistance of each cell in a module are measured and compared. The resistance is further characterized with pulse tests at various SOCs and ambient temperatures for a single cell to craft a simple loss model of the overall battery pack to answer the question: *How*

high is the power capability of a state-of-the-art battery electric vehicle in different usage scenarios. From an energy efficiency perspective within the electric powertrain, the powertrain unit (i.e., electric machine and inverter) is the most important lever to increase the vehicle efficiency. Therefore, powertrain tests are performed at the vehicle level to shed light on the questions: *How high are energy losses in the overall powertrain of current electric vehicles? Which impact do these losses have? Which levers exist to improve the overall efficiency?*

4.1. Capacity of the battery cells

The electro-thermal behavior of the battery cell under charge/discharge procedures from C/10 to 3C is illustrated in Fig. 9. At first glance, a steep overvoltage increase can be observed in the charge and discharge sequences (Fig. 9(a)/(b)). In the range of C/10 to 1C, the cell's overpotential approaches upper voltage limits earlier than lower voltages, indicating that in this operating window charging kinetic limitations may dominate discharge kinetics. Interestingly, the charge and discharge sequence seem to be both equally limited at current rates beyond 1C, as the CC charge and energy throughput reduce to less than 50% in comparison to the nominal capacity (Fig. 9(e)/(f)). This behavior seems reasonable, as high energy density cells suffer from large concentration gradients if graphite electrodes are used, leading to large overpotentials and reaching the voltage bounds early [35]. The risk of lithium deposition may be therefore aggravated and the fast charging capability limited. Taking into account the cell temperature evolution in Fig. 9(c)/(d), heat losses during discharge exceed the cell heat losses in charge direction; in particular beyond 1C. While low current rates up to 1C do not significantly increase the cell temperature in both charge and discharge direction, larger current rates lead to peak temperatures up to 40 °C and 52 °C for charge and discharge, respectively. Entropy of the active materials, as determined by previous studies [36], as the main origin for the large temperature difference is unlikely. In discharge scenarios, heat losses reach their maxima at the end of the discharge sequence during the CV phase, which stands in contrast to the charge sequence reaching the temperature maxima at the start of the CV phase. This observation may indicate that the impedance has a larger increase in low SOC regions, whereas it stays almost constant in high SOC regions. Low SOC regions are reached quickly during discharge, indicated by the nonlinear voltage drop before the start of the CV phase. Therefore, the impedance at varying SOC is further analyzed later on in Section 4.2. However, it remains unclear, if the discharge capability at 2C is strictly limited by the cell kinetics or whether the preceding 1C charge sequence already damaged the cell, e.g., by excessive lithium deposition, as only one cell has been used for the overall experiment.

It is worth emphasizing that the temperature difference between the anode and cathode temperature measurement quickly exceeds 5 K in the scenarios beyond 1C, which is on a par with the reported temperature evolution in the literature [37]. High rates may therefore lead to an inhomogeneous temperature distribution across the large cell length, which has been reported to cause hazardous aging mechanisms, e.g., lithium deposition [38]. Moreover, the tab temperatures achieve the largest temperature difference during aggressive cycling, with up to 10 K during a 3C discharge.

4.2. Resistance of the battery cells

Fig. 10 shows the dependency of the cell's resistance on the SOC, temperature, C-Rate, and pulse duration. The resistance at 50% SOC, 20 °C, −1 C, and 10 s was chosen as a reference to show the dependency of the influencing parameters. In this condition, the reference resistance of the battery cell was determined as 1.857 mΩ.

From Fig. 10(a) it becomes visible that the resistance's SOC dependency is larger for longer pulse durations. Whereas $R_{\mathrm{DC},1\ \mathrm{ms}}$,

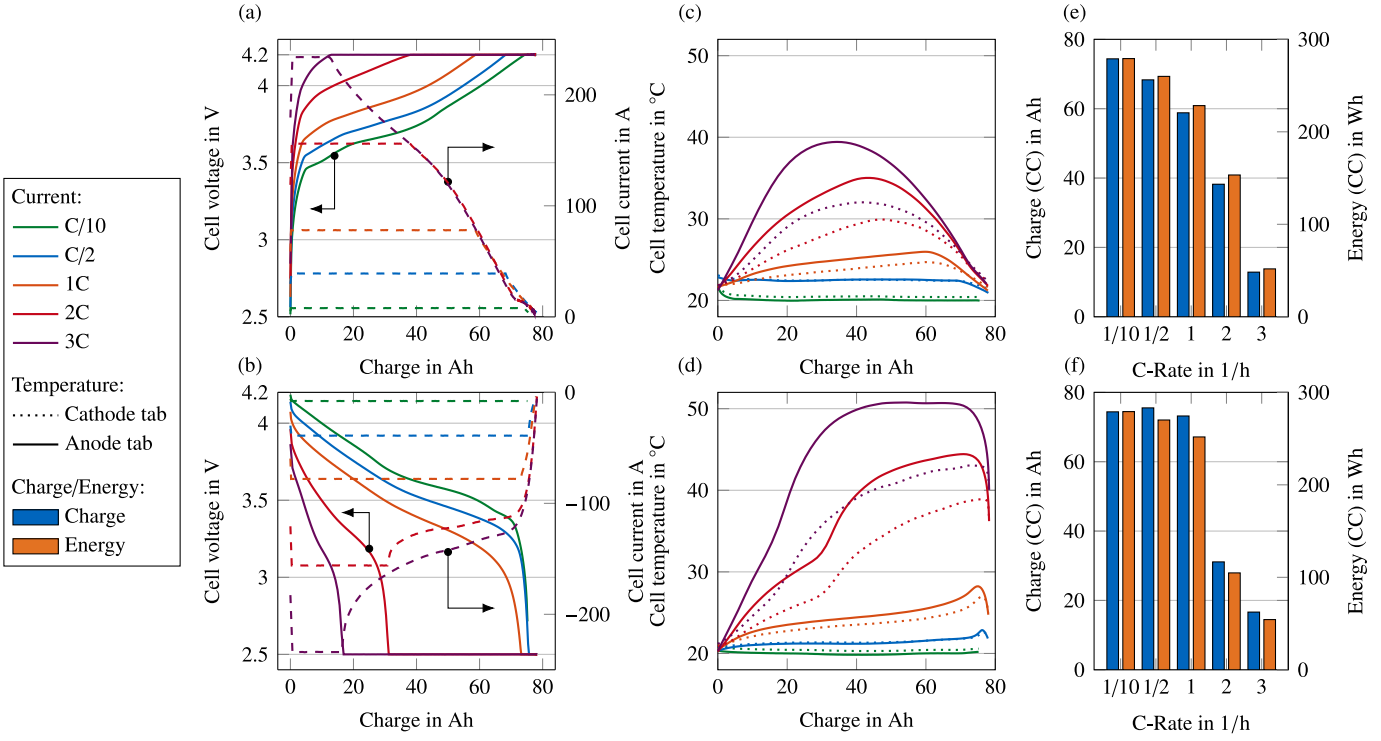

Fig. 9. Current rate tests of the battery cell under study. Voltage, current and temperature during (a)/(c) charge and (b)/(d) discharge. (e)/(f) CC charge and energy throughput at different current rates for charge and discharge, respectively. Note that the temperature signal has been post-processed with Savitzky-Golay filtering to reduce the measurement noise for visualization purposes.

which displays the Ohmic resistance, remains rather constant over SOC. $R_{DC,10\ s}$ for example increases towards a low SOC and in the mid-SOC area between 50% SOC and 70% SOC. This can be explained by dynamic loss processes such as the solid electrolyte interphase (SEI), charge transfer, and diffusion, which take effect at longer pulse durations [39]. The characteristic SOC dependency of these processes coincides well with the stage transitions of graphite, which were analyzed by DVA in Fig. 6, and can be explained by the homogenization effect in these areas [39]. Since the resistance depends strongly on the pulse duration due to the different occurring loss processes, knowledge about the expected frequency spectrum during the vehicle's operation is important.

Fig. 10(b) shows the resistance over SOC for different temperatures and Fig. 10(c) shows the resistance over temperature for different pulse durations. Again, the Ohmic resistance, observed at the 1 ms pulse duration, stays almost unaffected by varying temperatures, while for longer pulse durations, the exponential relationship between resistance and temperature (Arrhenius dependency) is revealed [40]. The strong increase of the resistance at low temperatures is of major importance, since it reduces the power capability of the battery system during vehicle operation under such temperature conditions.

In Fig. 10(d), the dependency of the resistance on the C-Rate is illustrated for different temperatures and for two different pulse durations: 1 ms and 10 s. Also here, the Ohmic resistance is affected little by the C-Rate, even for low temperatures. For $R_{DC,10\ s}$, the dependency of the C-Rate becomes more pronounced at 0 °C, leading to decreasing resistances with higher currents both in charge and discharge direction. These observations are in accordance with the Butler-Volmer equation describing the charger transfer kinetics of lithium intercalation [41]. Compared to the other influencing parameters, however, the dependency of the resistance on the C-Rate is rather small.

4.3. Parameter scattering within the battery module

Finite accuracy during the lithium-ion battery manufacturing process results in minimal differences in material compositions, overall component connectivity, and electrode thickness, among other factors [42,43]. These variations lead to different cell capacities, impedances, and self-discharge rates, which can affect the power of the entire battery pack system [44–47]. Especially for battery packs with numerous cells, the probability of a negative outlier increases.

Fig. 11(a)–(c) shows the measured capacity, impedance, and corresponding variation coefficient between the cells incorporated in the present module assembly. It was assumed that all cell parameters in this work are normally distributed and thus can be described by the mean value μ and standard deviation σ. All 24 cells show capacities C above the manufacturer's specification of 78 Ah, with a median of 79.06 Ah. The variance between the cells is small, as the coefficient of variation ($\kappa = \sigma/\mu$) amounts to 0.44% with a standard deviation of $\sigma = 0.3446$Ah and a mean of $\mu = 78.96$Ah. The impedance R_{Ohm} (corresponding to the zero-crossing at -Im(Z)) varies between 1.004 and 1.092 mΩ with $\mu = 1.051$ mΩ and $\sigma = 0.0283$ mΩ, resulting in $\kappa = 2.69\%$. For the charge transfer resistance R_{CT} (calculated from the local minimum of the imaginary part of the EIS Nyquist-Plots minus R_{Ohm}, also compare the marked area in Appendix F), the coefficient of variation amounts to 5.29% ($\mu = 0.341$ mΩ, $\sigma = 0.0180$ mΩ). The lowest capacity of 78.22 Ah is found in Cell-ID 1 at the boundary of the cell stack, the highest value of 79.55 Ah is present in the central part of the module.

Between C and R_{Ohm}, the Pearson product-moment correlation coefficient (PPMCC) (a measure of the linear dependency between two data sets, and specifically the strength of a linear association of

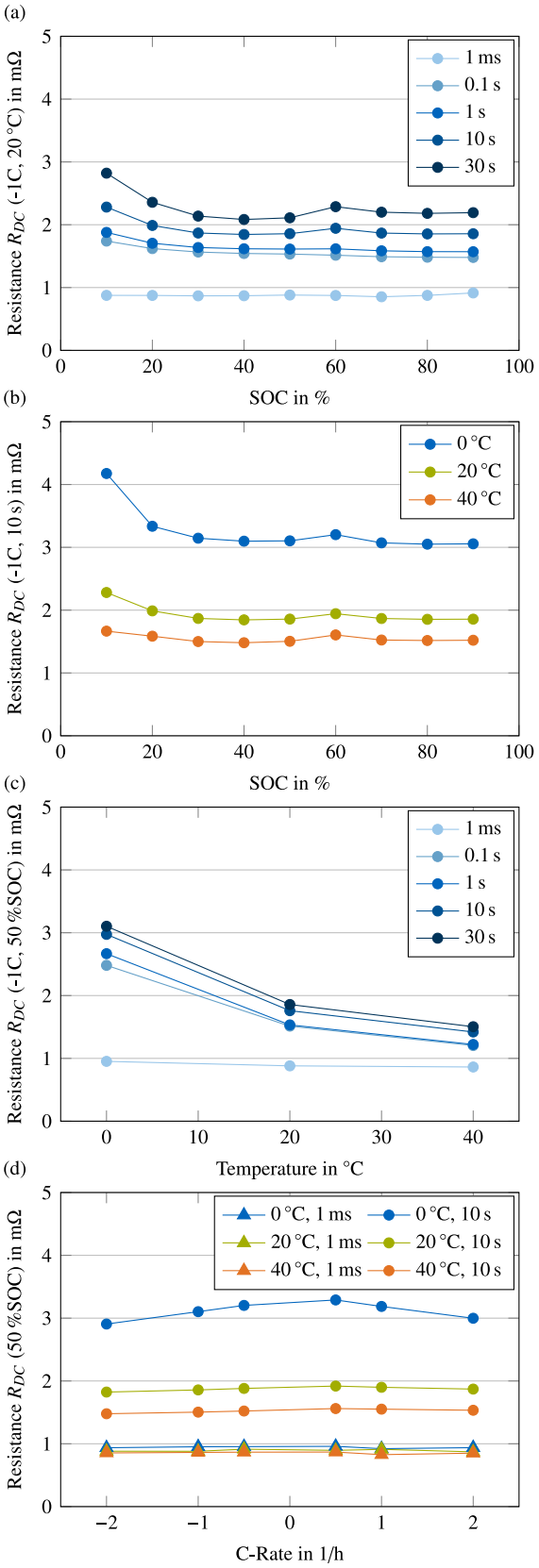

Fig. 10. Resistances R_{DC} of the battery cell under study. The resistance at 50% SOC, 20 °C, –1 C, and 10 s serves as a reference operating point. (a) Resistance over SOC for different time intervals. (b) Resistance over SOC for different temperatures. (c) Resistance over temperature for different time intervals. (d) Resistance over C-Rate for different temperatures and pulse durations.

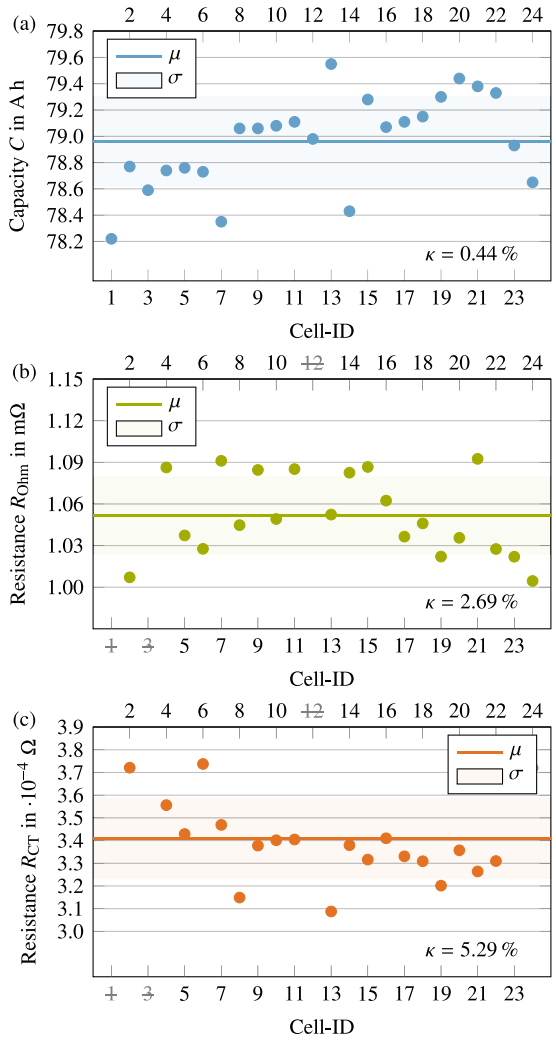

Fig. 11. Parameter scattering of the battery module. (a) Capacity C, (b) impedance R_{Ohm}, and (c) charge transfer resistance R_{CT} determined with C/3 CCCV discharge procedures between 2.5 V and 4.2 V and EIS measurements between 0.01 Hz and 5000 Hz at 20◦ ± 0.2 °C ambient temperature, plotted over the cell number. In plots (b)–(c), the measured data of cells 1, 3, and 12 were not taken into account because these cells had already undergone extended aging as a result of previous experiments. However, in a pre-test, we were able to validate that these cells are also within the scatter range of the cells shown.

a sample of paired data) is −0.0446, indicating no sufficiently present correlation [48]. A moderate correlation is evident between C and R_{CT} with a PPMCC of −0.6444. In contrast, the PPMCC of R_{Ohm} to R_{CT} is −0.3383, indicating a weak correlation between the data sets. No interpretation of the PPMCC values between the parameters will be given here, since these depend strongly on the measurement method and the chronology of the measurements [49].

In principle, the scattering shown may have its cause in initial variations in the cell characteristics (ex-factory) or differently aged cells. The latter would be due to the occurrence of deviating cumulative charge throughput, different SOC, or due to thermal effects in the module structure, such as stronger heat transfer and the influence of the cell position in the stack. As the cells are almost new and were precisely charged to 50% SOC before the EIS sweep, the present variations seem to be initial ones.

In order to draw statistically supported conclusions about the general production quality and dispersion, a sample size several orders of magnitude larger would be required (especially due to cell-screening at the manufacturer prior to delivery [50]). Nevertheless, the measured variation in capacity is consistent with values in the literature ranging from 0.16% to 0.80% [49,51–58]. The measured variance at R_{Ohm} exceeds values in the literature, e.g., 1.28% [52] and 1.94% [51], which may be due to the measurement setup involving the large-format, low-impedance cells, where inductivities cannot be completely avoided. The measured spread of R_{CT} is comparatively high, but the proportion of R_{Ohm} to R_{CT} can also be found in the literature [49,52]. This phenomenon may be partially explained by a higher temperature dependence of the charge transfer resistance than the Ohmic resistance [49,59]. Whether the arrangement of the cells in the module was chosen deliberately (based on their capacity or impedance values) cannot be ascertained without information from the manufacturer. Collectively, the picture of the scatter of all studied parameters is in good accordance with recent literature. For further visualization and analysis of the EIS results, the reader is referred to Appendix F.

4.4. Thermal management of the battery pack

Individual cell parameter variations and inhomogeneous cooling can lead to a temperature difference between individual battery cells inside the battery pack. This temperature difference leads to varying aging rates of the individual battery cells, which can increase inhomogenities even further. Because the powertrain efficiency, power capability and lifetime are determined by the weakest cell pair, it is crucial to minimize the thermal differences inside the battery pack.

In the following, we assess the thermal inhomogeneity of the battery modules in the battery pack during operation. For the evaluation we selected the most demanding cases in terms of thermal management engagement from Section 2.4.7. For driving or discharge conditions, the highway cycle possesses the highest velocity level and the most challenging power profile. Likewise, the DC fast charging event is chosen for harsh charge conditions. We subsequently analyzed the on-board recordings of the temperature sensors of the battery modules and the battery cooling inlet. In each module, two temperature sensors are located on the non-cooling side of the middle cell and the battery cooling inlet sensor is located close to the connection terminal of the cooling tube to the battery pack. To evaluate on the performance of battery thermal management systems (BTMSs), the proposed approaches in the literature are generally compared against a design threshold of 5 K temperature difference, which is seen as a critical threshold to prevent uneven aging in the battery pack [60–62]. To compare the proposed literature threshold to the present case, the temperature difference in the battery pack is calculated using

$$\Delta T = max(T_{\text{Module1}}, T_{\text{Module2}}, \ldots) - min(T_{\text{Module1}}, T_{\text{Module2}}, \ldots) \quad (4)$$

at each measurement time step for all nine modules. As all recordings are not labeled with the exact module number, sensor location cannot be distinguished. Therefore only the temperature difference in the pack, without additional information on the location, can be analyzed.

In the driving case, presented in Fig. 12(a)/(b), the temperature spread shows a maximum value of 1.4 K. The largest temperature differences can be observed at the points in which the temperature at the battery cooling inlet is dropping, which indicates that the battery cooling is activated. It can be observed, that in the driving case the active cooling is triggered, when the battery temperature exceeds a threshold of 32.5 °C. Before the shown driving sequence, the vehicle was 11 kW AC charged and, therefore, shows an initial temperature spread.

In the DC fast charging case, shown in Fig. 12(c)/(d), the temperature spread remains below 1.2 K until the temperature at the

cooling inlet reached its minimum at 21 °C. After this point, the absolute maximum temperature in the battery pack is reached and the temperature spread increases up to 1.9 K. With focus on the cooling strategy, it can be observed, that the minimal temperature at the cooling inlet is reached at a battery pack temperature level of approximately 42 °C.

It is shown that a DC fast charging event is more challenging from a thermal management perspective and in terms of temperature inhomogeneity. However, the temperature spread threshold of 5 K is not exceeded at any point during both events. The analyzed temperature spread represents the temperature difference between the modules and shows a dependence on the activation of the cooling system due to the heating of the coolant across the modules. It is therefore possible that a larger temperature spread prevails within a module due to thermal interaction between cells and different heat conduction to the environment. The different temperature levels at which the minimal temperature at the cooling inlet is reached indicates, that a higher temperature level is targeted in the fast charging event. This would stand in accordance to the findings in literature, which indicates that fast charging at elevated temperature levels increases the cycle life of the battery pack, avoiding malicious aging mechanisms [63–65]. In contrast, the minimum cooling temperature is reached faster in the driving case, highlighting the effort to keep the temperature strictly at a level of approximately 32.5 °C and minimizing the time span with active cooling, with regards to auxiliary power consumption.

4.5. Power capability of the battery pack

The achievable power capability of a battery is subject to design limits, which are implemented on the vehicle's BMS. These design limits avoid accelerated aging and safety-critical conditions by ensuring that the cell voltage and temperature limits are not violated. Avoiding excessive cell temperatures can be achieved by simply reducing the power limits at high temperatures. Staying within the voltage limits, however, requires taking into account the SOC and temperature of each cell in the pack.

To avoid violating the voltage limits, the voltage drop over the cell's internal resistance must not exceed the difference between the voltage limit and the OCV. Based on this voltage drop and the internal resistance of the cell, the maximum current can be calculated. The theoretical available power is then simply the product of the voltage limit and the maximum current. Since the OCV and internal resistance change with SOC, temperature and pulse duration, the available power is also a function of these parameters, according to

$$P_{ch} = \frac{U_{\max}(U_{\max} - U_{\mathrm{OCV}})}{R_{DC,ch}} \tag{5}$$

$$P_{dis} = \frac{U_{\min}(U_{\min} - U_{\mathrm{OCV}})}{R_{DC,dis}} \tag{6}$$

$$\text{where} \quad \begin{cases} U_{\mathrm{OCV}} = f(\mathrm{SOC}) \\ R_{\mathrm{DC,ch}} = f\left(\mathrm{SOC}, T, t_{pulse}\right) \\ R_{\mathrm{DC,dis}} = f\left(\mathrm{SOC}, T, t_{pulse}\right) \end{cases}$$

where P_{ch} and P_{dis} denote the maximum charge and discharge power, $U_{\max}$ and $U_{\min}$ the cell's maximum and minimum voltage limits, U_{OCV} the open-circuit voltage (OCV), T the cell's temperature, and t_{pulse} the duration of the current pulse. The upper and lower voltage limits were assumed to be 2.5 V and 4.2 V, corresponding to the conventional limits of an NMC-Graphite cell. The used OCV curve and impedance values correspond to the measurements presented in Figs. 6 and 10, respectively.

The resulting theoretical power limits are shown in Fig. 13. The power limits at the vehicle level are indicated at the right ordinate, which are obtained by multiplying the power limits of a single cell by the number of cells in the pack. The shown motor operating zone

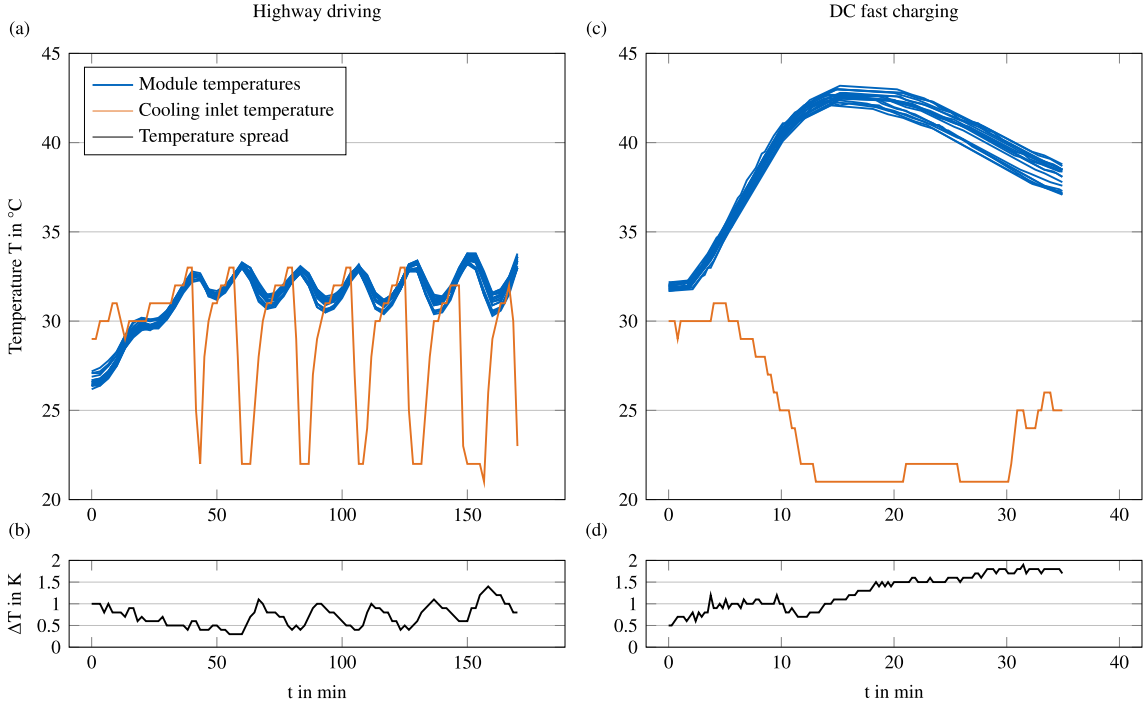

Fig. 12. Thermal management engagement and temperature recordings of the battery modules and the cooling inlet of the overall battery pack. Δ T is calculated between the maximum and minimum temperature in the battery pack at each sample point. (a)/(b) Repeated highway cycle on the dynamometer. (c)/(d) DC fast charging event recorded at a 350 kW charging pile.

is defined by the maximum power available for driving and recuperation. The annotations indicate the SOC at which the vehicle's available power becomes limited by the battery pack for different temperatures at a 30 s pulse duration. Note that positive power is defined as charging and negative power denotes discharging. A lower discharging power therefore correspond to a higher absolute discharging power.

The results show that the power limits are reduced as the pulse duration increases and as the temperature decreases, due to the increasing impedance of the cells. An opposite relationship between the power limits and the SOC is seen for charging and discharging. The charging power limits decrease with increasing SOC, whereas, the discharging power increases with increasing SOC. This is caused by the increasing open-circuit voltage with increasing SOCs, which reduces the gap to the upper voltage limit and increases the gap towards to the lower voltage limit.

In practice, a number of factors lead to a further reduction of the power limits. First, vehicle manufacturers will place a safety margin on the voltage limits to make sure the cells are not damaged during operation. Second, an upper limit to the temperature spread within a single cell may require reducing the power limits, depending on the heat transfer coefficient from the cell's core to the heat sink. Third, the power limits for the battery will be determined by the weakest cell in the pack. As shown in Fig. 12, the cells in the pack will reach different temperatures during operation. As a result, for cold batteries, the coldest cell will determine the power limits, whereas for hot batteries, the hottest cell will require the power limits to be reduced. This effect might be enhanced by the variation of the cell's capacities and internal resistances in the pack, as shown in Fig. 11, which may be amplified during the aging of the cell.

The presented theoretical power limits should therefore be interpreted as an upper bound. Nonetheless, a comparison with the installed propulsion power of 150 kW indicates that the vehicle's available power during driving for a pulse duration of 30 s is limited by the battery for SOC below 17.9% at a cell temperature of 0 °C. The ability to recover energy for 30 s is limited by the battery for SOC exceeding 55.9%, 73.0%, and 78% at temperatures of 0 °C, 20 °C, a 40 °C, respectively. A comparison with the charging power during a fast charging event, shown in Fig. 4, indicates that the implemented continuous charging power limits are not only determined by the cell's upper voltage limit, but also by the temperature and aging state of the battery cell and pack.

4.6. Electric powertrain efficiency

As the battery pack is only a minor limiter of the electric vehicle power capability, further analysis of the powertrain unit is performed. The efficiency from inverter input to motor output was calculated based on the mechanical power P_{mech} and the inverter power P_{inv} according to

$$\eta = \frac{P_{\mathrm{mech}}}{P_{\mathrm{inv}}} = \frac{T_{\mathrm{mot}} \cdot \omega_{\mathrm{mot}}}{(U_{\mathrm{bat}} \cdot I_{\mathrm{bat}}) - P_{\mathrm{aux}}}, \tag{7}$$

with the motor torque T_{mot}, motor speed ω_{mot}, battery voltage U_{bat}, battery current I_{bat}, and auxiliary power P_{aux}, including the compressor power for cooling. The measured efficiency map of the powertrain unit is illustrated in Fig. 14. Interestingly, despite the expected maximum rotation of 16.000 rpm, only approximately 14 000 rpm were recorded at maximum speed of the vehicle. In general, the maximum efficiency of 96% is achieved at around 9000 rpm and 140 Nm, emphasizing the need for right sizing and operation at high load for efficient operation. The efficiency stayed high at high power levels. For lower speeds, the efficiency dropped significantly in a neighborhood of below 4000 rpm.

In order to put all vehicle losses into context, we further differentiate between inverter-to-wheel-losses and wheel-to-distance-losses. The former includes inverter-, motor- and gearbox-losses as well as losses due to the friction brakes. The latter includes losses due to air and rolling resistance. The data acquisition was limited to dynamometer data and signals of the OBD-logger. Therefore, based on the fitted driving resistance of Equation (2), the wheel-to-distance-power P_{WtD}, and the resulting energy E_{WtD} can be calculated, which represent the required power and energy to overcome rolling and air resistance, according to

$$E_{\mathrm{WtD}} = \int_0^t P_{\mathrm{WtD}}\ \mathrm{d}t. = \int_0^t F_{\mathrm{fit}}(v) \cdot v\ \mathrm{d}t. \tag{8}$$

The measured battery output power P_{bat}, auxiliary power P_{aux} and the kinetic energy E_{kin} are used to determine inverter-to-wheel-losses, according to

$$E_{\mathrm{ItW}} = \int_0^t P_{\mathrm{bat}} - P_{\mathrm{aux}} - \frac{\mathrm{d}E_{\mathrm{kin}}}{\mathrm{d}t} - P_{\mathrm{WtD}}\ \mathrm{d}t \tag{9}$$

For E_{kin}, a rotational inertia factor of 1.03 and a driver and passenger mass of 150 kg is assumed. Battery losses within the battery are determined by

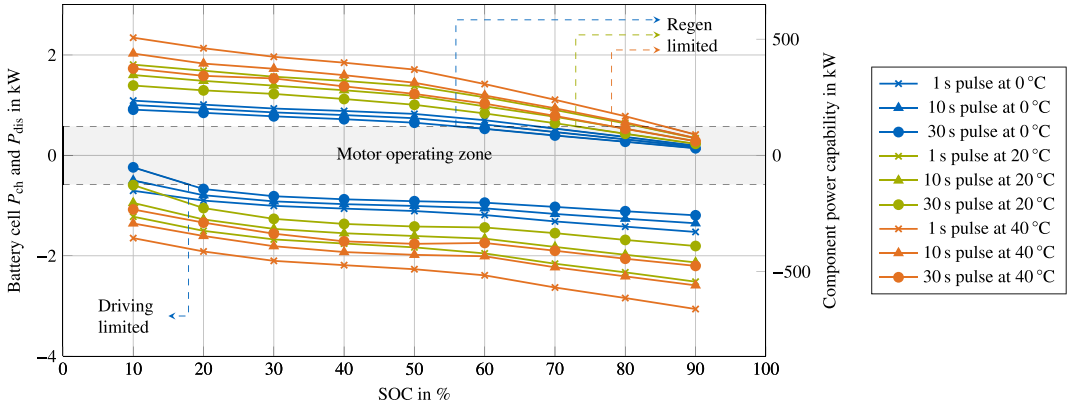

Fig. 13. Theoretical charging and discharging limits at cell level and vehicle level, alongside the vehicle's maximum motor power.

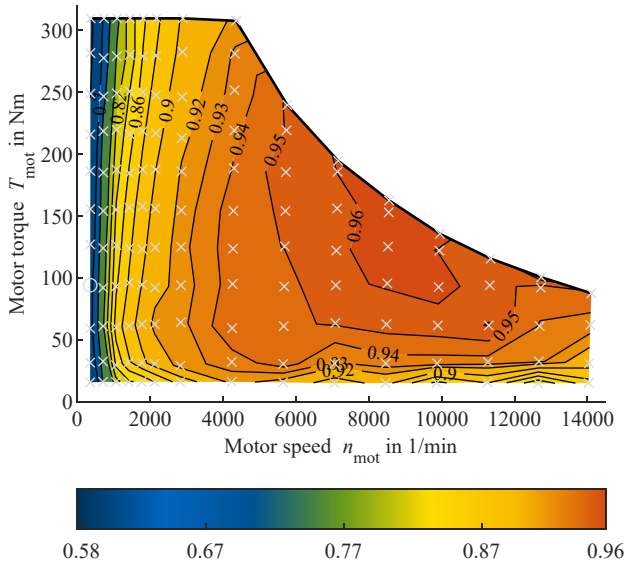

Fig. 14. Efficiency characteristics of the powertrain unit, i.e., inverter and electric motor, created with discrete measurement points and recorded on-board data. Base points are illustrated as crosses, excluded data points (due to implausibility) are illustrated as circles. Highly efficient driving situations of >96% are reached at high speeds of 8.000–10.000 rpm and high torques of >100 N m.

$$E_{\text{bat}} = \int_0^t \left(\frac{I_{\text{bat}}}{n_{\text{cell, par}}} \right)^2 \cdot R_{\text{i}} \cdot n_{\text{cells}} \, \mathrm{d}t \tag{10}$$

with $n_{\text{cell, par}}$ representing the number of parallel cells, n_{cells} the total number of cells. R_{i} is the internal cell resistance, which was set to 1.857 mΩ, based on the results from Section 4.2.

Fig. 15 shows the shares of wheel-to-distance, inverter-to-wheel and battery losses, as well as the energy consumed by auxiliary loads from the second run of the WLTP, urban, interurban and highway cycles. It can be seen that the distribution of losses significantly differs across the different driving cycles. Most of the energy is dissipated due to driving resistances (wheel-to-distance losses), highlighting the high energy efficiency of battery electric powertrains compared to other propulsion concepts. The largest share of losses within the powertrain can be traced back to the inverter-to-wheel losses, posing the need for improved design and operation strategies of these components to increase the efficiency and overall range of the vehicle. Especially in urban scenarios, in which the drag resistance is low and the powertrain unit is operated under partial load with low efficiencies, energy losses could be minimized by, e.g., optimizing or downsizing inverter-machine design to match the load points to high-efficiency regions.

It should be noted that the auxiliary power was low in these examples since the HVAC for cabin cooling/heating was inactive. Nonetheless, the auxiliary load is noticeable in the vehicle's energy consumption. Cooling power was only noticeable during the highway cycle. However, among all experiments, cooling power reached up to 3.14 kW in the investigated cycles and can influence energy demand for longer, more demanding trips at high temperatures. Based on the cycles, in which the cooling of the powertrain was active, it seems that the cooling strategy is set to keep the battery temperature under the threshold of 32.5 °C. Battery power losses contribute less than 4% to the overall power losses for the shown driving cycles.

The measurement accuracy at vehicle level is limited by the nature of the deployed methods. The presented data is collected by the OBD-II interface and complemented by calculated driving

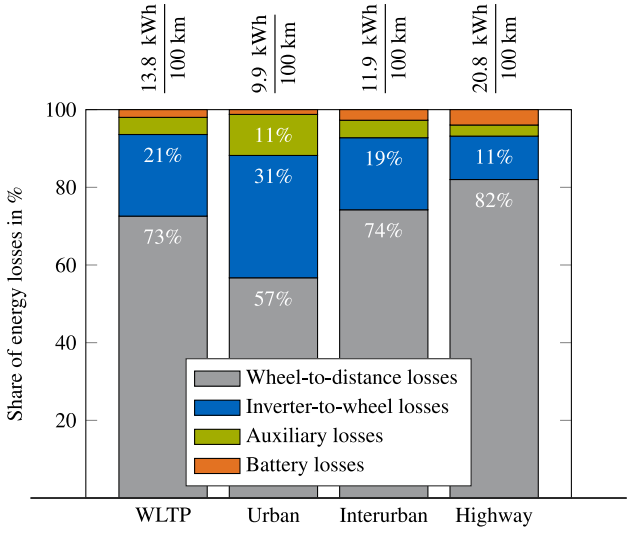

Fig. 15. Shares of different energy losses in the Volkswagen ID.3 for four driving cycles and total energy consumption.

resistance losses. However, it is not completely clear how accurate the onboard vehicle measurements are. Furthermore, signals such as the motor torque, are expected to be not directly measured within the vehicle but calculated onboard from other measurement sensors. This should be kept in mind in downstream analysis and usage of the presented data. Moreover, it has been observed that energy consumption reduces during repeated driving on the dynamometer, because of an unavoidable internal heat-up of the dynamometer components, which influences the provided resistance force. Dynamometer warm-up procedures were not possible due to the long charging times of the vehicle. To keep results comparable, all data points of Fig. 15 represent the second run of the respective sequence as the dynamometer temperature most accurately fits the temperature during the coast-down procedure.

5. Lifetime

Battery lifetime is the major lever on the sustainability of BEVs. In order to determine the lifetime of the battery cell and system under study, intensive aging tests are performed in order to answer the question: *How many cycles do state-of-the-art battery cells last?* The results are then projected to application level to yield an estimate of the mileage and get an answer to the question: *How many kilometers and years do state-of-the-art battery electric vehicles last?*

5.1. Real-world usage pattern

In addition to the experimental conditions, the charge/discharge scenario is also a decisive lever for a close-to-realistic aging of the battery cells. It is well known that different usage patterns strongly affect the battery aging speed, leading to an aging spread of similar battery packs during operation. This fact is indicated by Preger et al. [66] for different load spectra, i.e., different combinations of constant C-Rates, depth of discharge (DOD)'s, and temperature. Yuksel et al. [67] and Neubauer et al. [68] both investigated the impact of various driving behaviors and operation conditions employing aging models. They show an increase in capacity loss with higher driving aggression and higher ambient temperatures.

Therefore, we compose two edge cases from the measured charge and discharge dynamics under different vehicle situations to account for the most conservative and most demanding scenario. Both composed usage patterns and aging scenarios are presented in

Fig. 16. It should be noted that those usage patterns are applied to the cell utilizing the power demand resulting from the drive cycle measured on the dynamometer instead of the recorded current. Consequently, the applied load is independent of the battery state since the voltage and the impedance are not constant over the SOC range and the aging progress, respectively.

The first usage pattern is set to be a conservative scenario imitating modest urban or commuting usage starting from 80% SOC with a combination of the urban and interurban discharge cycle, summed up to 28 km, directly followed by an 11 kW AC charging sequence; all scaled to cell level. This pattern leads to a mean SOC of 76% and a delta DOD of 8% on cell level. The mean current during discharging amounts to −16.4 A and during recuperation to 16.0 A. Those values correspond to a mean C-Rate of around 0.2C in the course of the dynamic load profile. The maximum occurring currents are −133.1 A (1.7C) and 88.4 A (1.1C). The charge sequence causes a maximum current of 12.1 A (0.2C). Note that these C-Rates refer to the nominal capacity of the cell.

The second usage pattern is set to be an aggressive scenario imitating demanding long-distance usage starting from 100% SOC with the highway discharge cycle until 20% UI-SOC is reached, summed up to 375 km, followed by a 100 kW DC charging sequence up to 80% UI-SOC and again followed by the highway discharge cycle to 20% SOC. Every second charge event is a complete charge to 100% SOC with the 11 kW AC charging sequence, because no permanent usage of fast charging is to be expected and a recalibration point for the charge counter is necessary to avoid any drift of the measurement. The mean discharge current amounts to -36.1 A (-0.5C) whereas the mean recuperation current sums up to 19.3 A (0.3C). The maximum currents reach -190.0 A (-2.4C) in discharge direction and 135.5 A (1.7C) in charge direction respectively. The maximum charge current throughout the DC fast charge sequence is 121.2 A (1.6C) and during AC wallbox charging 14.2 A (0.2C). To account for an adaptive fast charging strategy without knowing the actual fast charging control, the DC fast charging current profile is approximated by a stair profile of successive CC charge commands, each terminated by a voltage limit. In this way, the current profile of the measured fast charge sequence is lowered based on the current state of health (SOH) of the cell, as it can be expected from the battery management in the vehicle. Thus, the cell is operated within safety limits at all times. Note that the operating SOC windows are set to the manufacturer's recommendations in both scenarios to exclude misuse of the operating instructions.

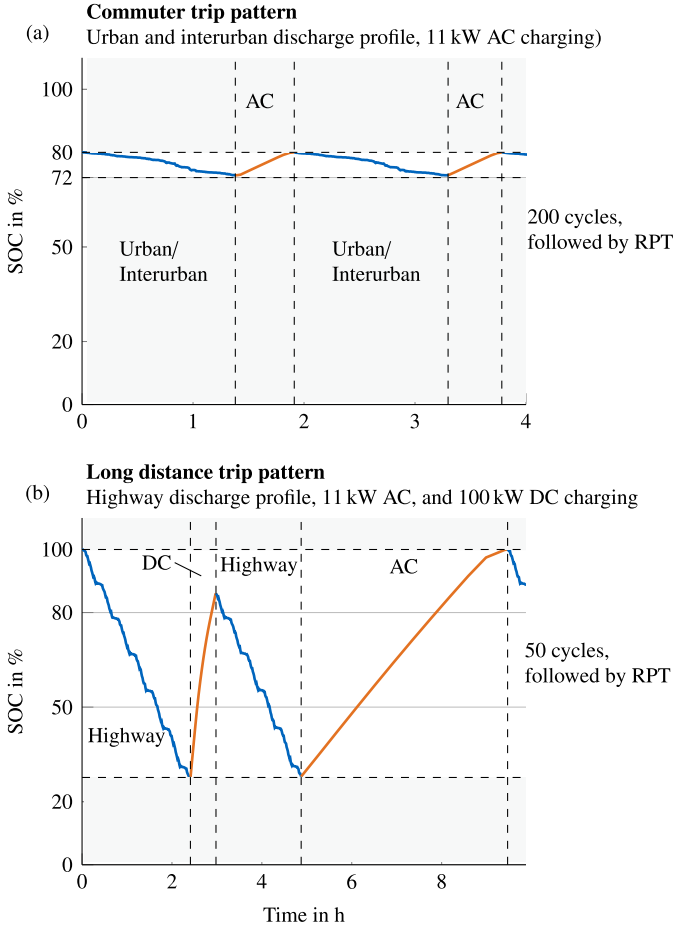

Fig. 16. Two usage edge cases composed from measured real-world cycles for accelerated aging tests. (a) Commuter trip pattern with a combination of the urban and interurban cycles, charged with the recorded AC charging profile. (b) Long-distance trip pattern with the Highway cycles and the DC charging profile every second charging event. Operating SOC windows are set to the manufacturer's recommendations to exclude misuse conditions. Note that illustrated SOCs represent the actual cell SOC, which is higher than the UI-SOC.

5.2. Cycle life

Fig. 17(a) provides capacity retention over equivalent full cycles (EFC) of the applied two use-case scenarios in comparison to a constant current cycling with 1C/1C and an excerpt of aging studies from the literature. One EFC is hereby defined as the ratio of the absolute charge throughput to the nominal capacity of the cell, i.e., one discharge and charge at 100% DOD yields one EFC. As earlier reported for C/NMC lithium-ion batteries in the literature [66], the capacity fade first follows a fast capacity drop and then follows a linear trend, until reaching a fast non-linear aging [69], often referred to as aging knee-point [70]. The aging trend of both scenarios first closely matches the expected trend from the literature values. However, in a later course, the aging rate is steadily limited in a way, that all curves show a trend to outperform the reported literature values. The highway use-case scenario accelerates the capacity fade rate over cycles by 16% compared to the commuter use-case scenario. This can be traced back to a larger capacity utilization due to increased cycling over almost the full DOD. Surprisingly, the accelerated capacity fade rate cannot be traced back in part to increased temperatures of the cell as initially assumed, as the measured peak temperatures in both scenarios do not differ significantly with a ~3 K peak temperature difference. This might diverge in reality, as battery pack temperatures due to multiple cells in operation cannot be replicated with the measurement setup.

It should be highlighted that a projected cycle life to a common EOL definition of 70%–80% SOH seems to outperform the to-be-believed cycle life of around 600–1000 EFCs of commercially available state-of-the-art C/NMC batteries [66,71–73]. The improved cycle life of the commuter use-case scenario should be kept in mind since the use-case scenario seems to be more realistic as the considered vehicle concept can be expected to be more likely used in urban areas than on long-distance trips. As the presented aging tests are intensively time-consuming, the tests are conducted further beyond the scope of this study and will be analyzed in a follow-up article with a more detailed analysis of the driving aging modes.

5.3. Mileage and operating time

Considering the data provided in Fig. 17(a), cycle life information is hard to interpret at vehicle level. Therefore, we aim to provide a more user-oriented mileage and operating time by projecting the achieved cycle life to the vehicle level, as visualized in Fig. 17(b). As the real-world cycles were actually driven with the vehicle under test, the driven absolute range can be used to yield a mileage

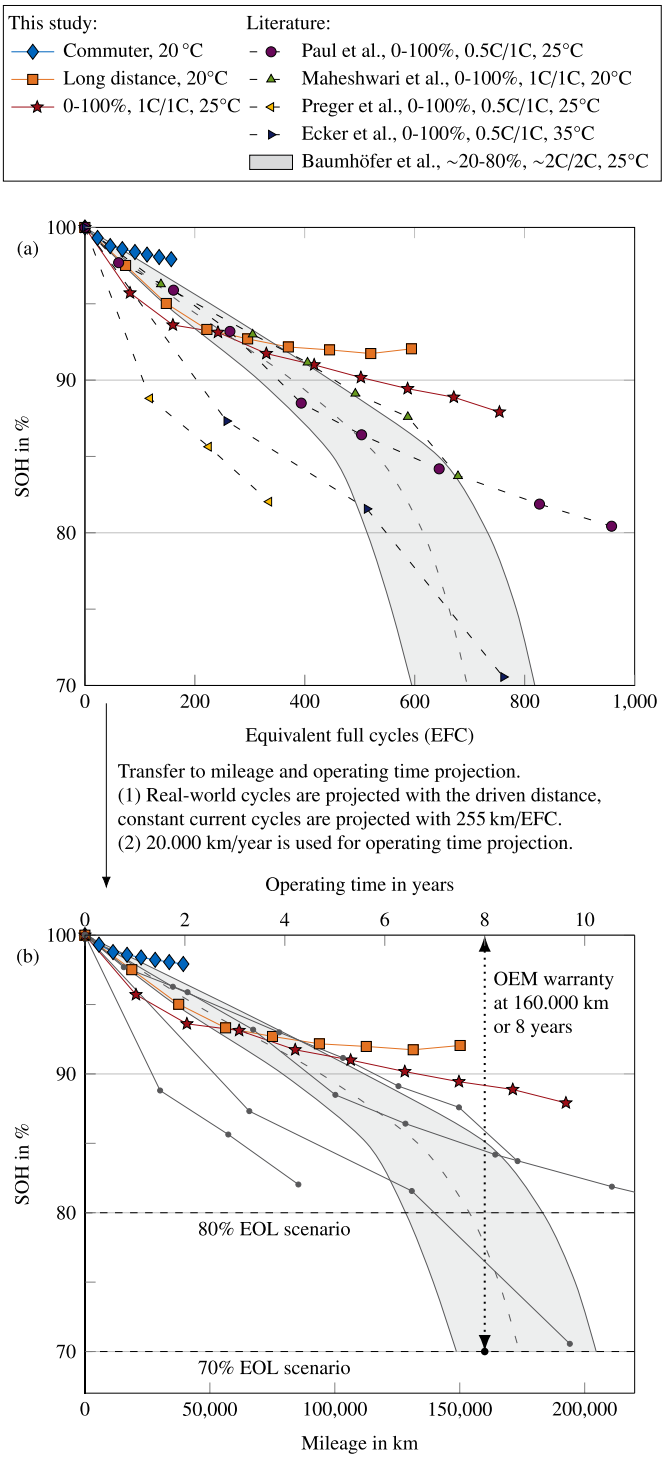

Fig. 17. Cycle life, mileage, and operating time prediction of the Volkswagen ID.3 battery cell under study. (a) Capacity loss over equivalent full cycles (EFCs) for the real-world use-cases compared to 1C/1C synthetic cycling and literature studies. (b) Mileage and operating time projection based on the cycle life results, different end-of-life scenarios, the actual achievable range of both usage patterns, and an average usage assumption of 20.000 km/year for all scenarios. Literature values are grey shaded for reference and estimated by multiplying with 255 km/EFC averaged from the real-world use-cases.

projection. Also, the data can be used to translate empirical studies with a ratio of 255 km/EFC based on the average of both real-world cycles. Further, we assume a common usage scenario of 20,000 km per year. Calendar aging due to idle times of the vehicle is neglected. Following this argumentation and assuming a similar trend, the battery can be expected to achieve a mileage and operating time far over the manufacturer warranty of 160,000 km and 8 years up to a SOH of 70%, with only approximately 8 % of capacity loss for the dynamic highway scenario up to the warranty limit, if operated under realistic conditions and according to the manufacturer guidelines. An early knee-point of the aging course with automotive A-grade cells, as measured with C-grade cells within the study of Baumhöfer et al. [69], is unlikely, which is why a trend of the capacity decay proportional to $\sqrt{Q}$ and, thus, $\sqrt{\text{EFC}}$ can be expected until 70% SOH, already visible in Fig. 17(b) and reported by previous studies in the field [74,75]. To support these assumptions with ground-truth data and exact figures, aging experiments are being conducted beyond the scope of this article and will be analyzed in a follow-up article, as stated in the previous section.

6. Summary, conclusions, and future work

This article presents an in-depth multi-scale assessment of a state-of-the-art automotive electric powertrain from the Volkswagen ID.3 Pro Performance at multiple levels. The vehicle has been acquired from a dealer to ensure we obtained an unmodified mass-series electric vehicle and to perform independent tests. A comprehensive investigation of the vehicle under study is presented discussing the achievements in the state of the art from different user-oriented perspectives, i.e. range, efficiency and sustainability. Overall, the key conclusions of this study can be summarized as follows:

- **Range deviations from standard cycles.**

The achievable electric range outperforms WLTP specifications in realistic urban to interurban scenarios, whilst the electric range is restricted in the realistic highway scenario. The main origin can be traced back to large wheel-to-distance losses by, e.g., the drag resistance, accounting for up to 82% of the total energy losses. Besides, the second-largest lever for an improved efficiency lies in the powertrain unit, which could be improved by larger advanced materials/technologies, e.g., such as the usage of SiC-MOSFET-Inverters, and improved thermal management strategies, e.g., by vehicle state-dependent thermal control windows during operation distinguishing between different driving and charging modes.

- **Component integration and energy density.**

While 273 Wh/kg and 685 Wh/L are achieved in gravimetric and volumetric energy density at cell level, energy density reduces to 233 Wh/kg and 530 Wh/L at module level and further reduces two-fold to 173 Wh/kg and 284 Wh/L at pack level. If voltage limits are considered, energy density further reduces by 7%. The results emphasize the need for a higher degree of battery cell integration without the need for battery modules by, e.g., cell-to-pack or cell-to-chassis concepts.

- **Power capability in different scenarios.**

In terms of power capability, analysis at varying temperatures showed that subzero temperatures are still challenging as power capability is strictly limited due to increased resistances at the cell level. This poses the need for advanced preheating strategies of the overall battery pack by, e.g., usage-specific preconditioning algorithms. During charging, the charging power seems to be limited at the cell level as C-Rates above 1C already led to a steep voltage increase. Advanced cell design and materials with either less overpotential tendency (e.g., thinner electrodes) or better thermal

stability (e.g., LFP) could improve the power capability, especially in the charge direction.

- **System effects on performance.**

The initial capacity and impedance deviations of the battery cells within the battery module are in good accordance with previously published deviations in the literature ($< 0.5\%$ for capacity and $< 3.0\%$ for internal resistance). During usage, thermal module-to-module gradients due to those deviations and the BTMSs are as low as ~2 K in the worst case 100 kW DC fast charging scenario. However, small differences lead to a more restricted voltage window of the overall system, which may amplify with the age of the battery pack and limit the available electric range. Moreover, with higher charging power in the future, these deviations may spread further and should be counteracted by advanced thermal management of the cells by, e.g., a more direct and powerful waste heat dissipation at the source of origin.

- **Battery cycle life and mileage projection.**

Aging tests showed a reduced aging rate compared to figures reported in the literature. In total, the real-world cycles far outperform the mileage and operating time warranty by the manufacturer and assumptions generally taken in the literature. If these updated numbers are considered in electric powertrain concept comparisons, such as in the intensively discussed fuel cell versus battery-electric debate, battery electric vehicles may be more superior than previously assumed. We, therefore, strongly advice to account for these updated results of the follow-up article on the absolute aging results, especially in life cycle assessments (LCAs) and total cost of ownership (TCO) studies.

Future work will include the usage of the results as a reference, benchmark, and starting point to research activities. We encourage researchers to use the underlying open-source dataset for their studies. Additional BEVs, such as a Tesla Model 3 Standard Range (C/LFP), will be analyzed in a subsequent study and compared to the results of the underlying article. Also, the battery aging in different scenarios will be analyzed in more detail in a follow-up study.

Data availability

We want to give any researcher access to our measurement data without any limits. Over 10 GB of measurement data of the article are provided as an open source, accessible via mediaTUM: https://doi.org/10.14459/2022mp1656314 Additionally, almost 150 real-driving cycles of the vehicle under study are provided as open source, accessible via mediaTUM: https://doi.org/10.14459/2022mp1656313.

CRediT authorship contribution statement

Nikolaos Wassiliadis: Conceptualization, Methodology, Investigation, Resources, Writing – original draft, Visualization, Writing – review & editing, Project administration, Funding acquisition. **Matthias Steinsträter:** Methodology, Investigation, Writing – original draft, Writing – review & editing, Project administration. **Markus Schreiber:** Investigation, Writing – original draft, Writing – review & editing, Visualization. **Philipp Rosner:** Investigation, Writing – original draft, Writing – review & editing, Visualization. **Lorenzo Nicoletti:** Investigation, Writing – original draft, Writing – review & editing, Visualization. **Florian Schmid:** Software. **Manuel Ank:** Investigation, Writing – original draft, Writing – review & editing, Visualization. **Olaf Teichert:** Investigation, Writing – original draft, Writing – review & editing, Visualization. **Leo Wildfeuer:** Investigation, Writing – original draft, Writing – review & editing, Visualization. **Jakob Schneider:** Investigation, Writing – original draft, Writing – review & editing, Visualization. **Alexander Koch:** Investigation, Writing – original draft, Writing – review & editing, Visualization. **Adrian König:** Investigation, Writing – original draft, Visualization. **Andreas Glatz:** Investigation, Writing – original draft, Visualization. **Josef Gandlgruber:** Investigation, Writing – original draft, Visualization. **Thomas Kröger:** Data curation. **Xue Lin:** Writing – review & editing. **Markus Lienkamp:** Resources, Supervision, Writing – review & editing, Funding acquisition.

Declaration of competing interest

The authors declare that they have no known competing financial interests or personal relationships that could have appeared to influence the work reported in this paper.

Acknowledgment

We want to thank Florian Biechl and the staff of the electrical workshop, as well as Erwin Darnhofer and the staff of the mechanical workshop for their aid and advice during the experimental investigation. This project has been partly funded by the German Federal Ministry of Education and Research (BMBF) within the projects “BALd” under grant number 03XP0320B, “BetterBat” under grant number 03XP0362C, “OptiPro” under grant number 03XP0364B, “UNICARagil” under grant number 16EMO0288, partly funded by the German Federal Ministry for Economic Affairs and Climate Action (BMWK) within the projects “NEFTON” under grant number 01MV21004A, “ultraBatt” under grant number 01MV21015D, and partly funded by the Bavarian Ministry of Economic Affairs, Energy and Technology within the project “KIBA” under grant number DIK-0123/01.

A Vehicle specifications

The vehicle specifications of the battery electric vehicle under study are provided in Table A.

Table A
Overview of vehicle specifications of the Volkswagen ID.3 Pro Performance under study. Data is collected from the Certificate of Conformity (COC) according to EU Regulation 2018/858 [16], vehicle registration documents, previous material analysis of the battery cell [22], and assumption based on media and press releases.

Domain	Attribute	Value	Unit
Vehicle	Range (WLTP)[c]	408	km
	Max. speed[c]	160	km/h
Vehicle	Mass[c]	1794	kg
	Actual mass[c]	1891	kg
	Tyres[c]	215/45 R20 95T	–
	Tyre radius[m]	346.8	mm
	Road load coefficient – f0[c]	110.0	N
	Road load coefficient – f1[c]	0.855	N/(km/h)
	Road load coefficient – f2[c]	0.02445	N/(km/h)^2
Power unit	Max. power[c]	150	kW
	Cont. power (30 min)[c]	70	kW
	Max. rotations[a]	16000	1/min
	Max. torque[r]	310	N m
	Drive type[a]	PSM	
	Inverter[a]	IGBT	
	Gearing ratio[c]	11.53:1	–
Battery unit	Pack energy[r]	58	kWh
	Cell capacity[l]	78	Ah
	Cell format[l]	Pouch	–
	Chemistry[l]	C/NMC	–

[m] Determined by measurements.
[c] Taken from the Certificate of Conformity (COC).
[r] Taken from the vehicle registration documents.
[l] Taken from the literature, i.e., Ref. [22].
[a] Assumptions taken from media and press releases.

B UDS IDs and physical interpretation

All recorded signals from onboard measurements are summarized in Table B.

Table B
Overview of an excerpt the acquired signals from UDS requests via the OBD-II interface of the investigated Volkswagen ID.3.

Control device name	Control device ID	Signal name	Signal ID	Start-Bit	Data length	Conversion	Unit
High Voltage Battery	0x17FC007B	Pack voltage	0x1E3B	24	16	0.25	V
	0x17FC007B	Pack current	0x1E3D	24	16	0.01−1500	A
	0x17FC007B	SOC	0x028C	24	8	1/255	%
	0x17FC007B	Voltage cell 1	0x1E40	24	16	0.001 + 1	V
	0x17FC007B	Voltage cell 2	0x1E41	24	16	0.001 + 1	V
	⋮	⋮	⋮				
	0x17FC007B	Voltage cell 107	0x1EAA	24	16	0.001 + 1	V
	0x17FC007B	Voltage cell 108	0x1EAB	24	16	0.001 + 1	V
	0x17FC007B	Coolant inlet temperature	0x2A0B	24	8	0.15625	°C
	0x17FC007B	Battery temperature 1	0x1EAE	24	16	0.1−27.315	°C
	⋮	⋮	⋮				
	0x17FC007B	Battery temperature 16	0x1EBD	24	16	0.1−27.315	°C
	0x17FC007B	Battery temperature 17	0x7425	24	16	0.1−27.315	°C
	0x17FC007B	Battery temperature 18	0x7426	24	16	0.1−27.315	°C
	0x17FC007B	Cumulative charge	0x1E32	128	32	0.00011650853	kWh
	0x17FC007B	Cumulative discharge	0x1E32	96	32	0.00011650853	kWh
Inverter	0x17FC007C	Mileage	0x086D	24	32	1	Km
	0x17FC007C	Intermediate circuit current	0x3E98	24	32	float	A
	0x17FC007C	Intermediate circuit voltage	0x43B9	24	32	float	A
Electric machine	0x17FC0076	Vehicle speed	0x2B16	24	16	0.01	km/h
	0x17FC0076	Axle actual torque	0x033B	24	16	1	Nm
	0x17FC0076	Electric machine rotations	0x3DF8	24	16	0.5	1/min
	0x17FC0076	Power auxiliary devices	0x0364	24	16	100	W
	0x17FC0076	Stator temperature	0x4672	24	32	float	°C

Note that the acquired data is recorded at a data acquisition rate up to 105 Hz in total and shifted between the different signals according to (1) the desired data acquisition rate of a specific signal and (2) the UDS data transmission capability of a specific electronic control unit (ECU).Extended Diagnostic Session may be required. Float is interpreted as an IEEE 754 single-precision floating-point number.

C Coast-down procedure and driving resistance regressions

Figure C(a) shows the measured velocity of the coast-down of the vehicle on the dynamometer and on the test track. For improved statistical safety and to eliminate uneven road surfaces, the procedures were performed three times in each direction. The remaining deviations can be argued by the unavoidable unevenness of the test track and the fact that the individual speed ranges had to be subdivided because of the short track length. This leads to curvature errors, since the dynamometer does not simulate any slope. The target coefficients of the vehicle are determined by evaluating the coast-down curve from the test track ($a_0 = 121.7$ N, $a_1 = 4.62$ N/(m/s) and $a_2 = 0.275$ N/(m/s)^2). Since part of the driving resistance still exists on the dynamometer, those parameters need to be adjusted to transfer the real driving behavior to the chassis dynamometer. This was done iteratively, until both curves reaches a satisfactorily low error. We then refer to the resulting coefficients as $a_0 = 54.1$ N, $a_1 = 3.48$ N/(m/s) and $a_2 = 0.295$ N/(m/s)^2. Furthermore, we compare the coast-down curve with the curve provided by the manufacturer (Table A). Figure C(b) shows that the curves fit well and only have small deviations at lower speeds. This is probably due to deviations from the optimum measurement conditions during the performed coast-down test in comparison to the manufacturer, but can be tolerated for the underlying study as deviations are expected to remain small.

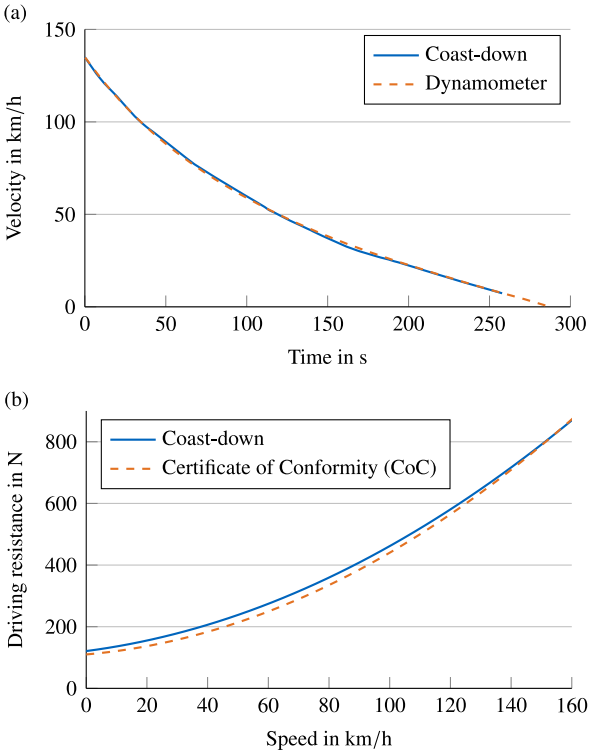

Fig. C. Coast-down measurements. (a) Coast-down velocity over time measured on the test track and on the dynamometer. (b) Driving resistance measured on the test track compared to data from the Certificate of Conformity (COC).

D Open-circuit voltage determination

As mentioned previously, C/10 and C/50 charge and discharge pOCV measurements have been conducted on the cell level at 20 °C ambient temperature, as has a galvanostatic intermittent titration technique (GITT). The latter incorporated 2.5% SOC steps with C/10 CC pulses and a relaxation time of 6 h at 0–30% SOC, 4 h at 30–45% SOC, and 2 h at 45–100% SOC in both current directions. Figure D shows the determined OCV derived from the aforementioned methods.

In general, the pOCV and GITT measurements show a good fit in the OCV curve. In DVA, both the C/10 and C/50 measurement generally show similar behavior to the C/40 curve analyzed in Subsection 3.1. However, both the C/10 half-cycles show an interesting additional double feature (magnified in Figure D) which is more pronounced for charging. Compared to where a silicon plateau is to be expected, it occurs at a lower SOC of around 4% and a higher normalized differential voltage of 0 V. As it is already visible in a close comparison of all four raw pOCV curves, smoothing errors and relaxation issues could be excluded as suspect causes. In a small SOC range, the C/10 absolute discharge voltage even surpasses that of the C/50 cycle. The feature's origin could not be ultimately determined, but its disappearance in the lower current measurements point away from a thermodynamic background (i.e., cell chemistry) and more towards dynamic effects or testing artifacts.

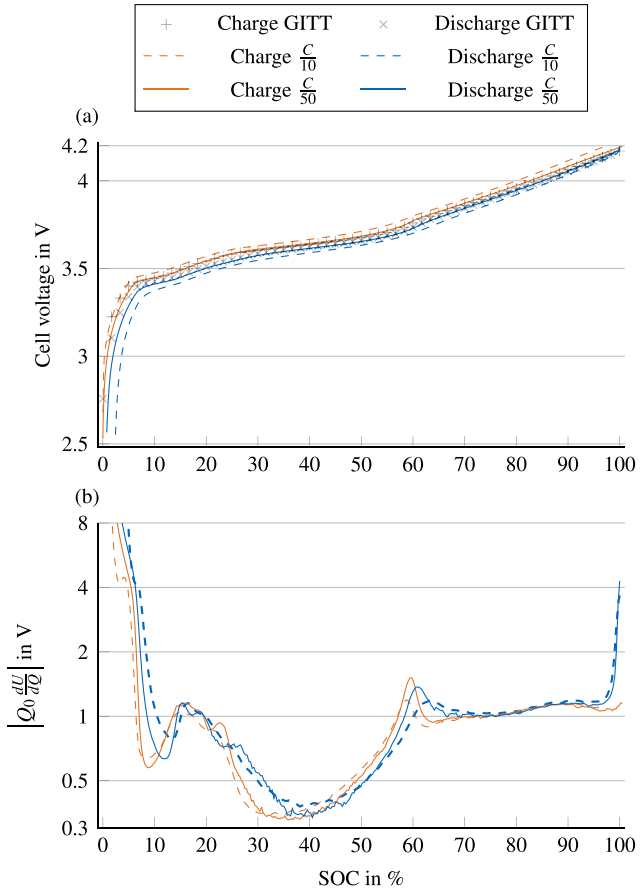

Fig. D. Open-circuit voltages determined with different methods. (a) pOCV at C/10, pOCV at C/50, and GITT to determine the OCV. (b) DVA of the pOCV procedure.

E Energy density across multiple levels

Table E
Overview of the energy densities of the vehicle under study from the cell to vehicle level.

Level		Cell	Module	Pack	Pack	Unit
		Measured	*Scaled*	*Scaled*	*Measured*	
Architecture	Parallel	1	2	2	2	
	Serial	1	12	108	108	
Datasheet specifications	Charge	78	156	156	156	Ah
	Energy	0.285	6.850	58	58	kWh
Energy	Charge	80.445 [m]	160.889	160.889	149.530 [m]	Ah
	Energy	0.300 [m]	7.207	64.862	60.610 [m]	kWh
	Upper voltage limit	4.2 [m]	50.4	453.6	452.0 [m]	V
	Lower voltage limit	2.5 [m]	30	270.0	359.3 [m]	V
Volume	Height	98 [m]	222 [m]	129 [m]	129 [m]	mm
	Length	515 [m]	589 [m]	1317 [m]	1317 [m]	mm
	Thickness	8.7 [m]	107 [m]	1448 [m]	1448 [m]	mm
	Volume	0.438	13.6	228.2	228.2	L
Mass		1.101 [m]	30.92 [m]	375.0 [m]	375.0 [m]	kg
Energy density	Gravimetric	273	233	173	162	Wh/kg
	Volumetric	685	530	284	266	Wh/L

[m] Determined by measurements.

Table E gives an overview of the calculated energy densities across multiple integration levels of the battery. Values are partly scaled and partly measured, as indicated. Both, cell and pack charge/energy measurements, are based on a C/40 CC charge sequence between the stated voltage bounds. All integration levels, i.e., cell, module, and pack, have been weighed and the geometry measured to calculate the gravimetric and volumetric energy density. Predominantly, energy density losses from cell via module to pack level occur due to inactive material (e.g., housings, electrical equipment). The energy density losses from the last step occurred due to voltage limits set by the battery management system.

F Electrochemical impedance spectroscopy

The presented EIS measurements of the cells are further visualized in a Bode and Nyquist diagram in Figure F. The excitation signal of 4 rms mV was selected in order not to exceed the limits of the measuring equipment. The sense and source wires were routed away as independently as possible. Due to the large-format, low-impedance cell, effects caused by the measurement setup, especially in the high-frequency range, cannot be entirely ruled out. It was ensured that the tests were carried out under

constant environmental conditions at a temperature of 20◦.

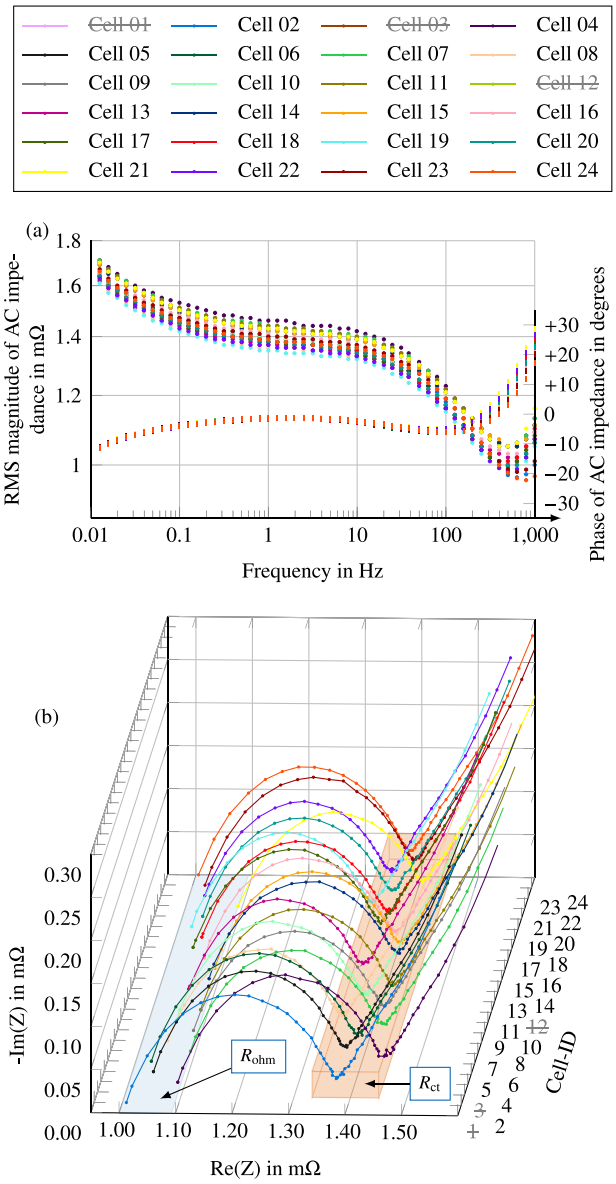

Fig. F. Superimposed EIS measurements of the cells in the module, section from ~1 kHz to 0.01 Hz. (a) Bode-Plot and (b) Nyquist-Plot.

References

[1] International Energy Agency, Global EV Outlook. Accelerating ambitions despite the pandemic. URL, https://www.iea.org/reports/global-ev-outlook-2021; 2021. Accessed at 24 December 2021.

[2] König A, Nicoletti L, Schröder D, Wolff S, Waclaw A, Lienkamp M. An overview of parameter and cost for battery electric vehicles. World Electr. Veh. J. 2021;12(1):21. https://doi.org/10.3390/wevj12010021.

[3] van Mierlo J, Berecibar M, El Baghdadi M, de Cauwer C, Messagie M, Coosemans T, Jacobs VA, Hegazy O. Beyond the state of the art of electric vehicles: a fact-based paper of the current and prospective electric vehicle technologies. World Electr. Veh. J. 2021;12(1):20. https://doi.org/10.3390/wevj12010020.

[4] Blomgren GE. The development and future of lithium ion batteries. J Electrochem Soc 2017;164(1):A5019–25. https://doi.org/10.1149/2.0251701jes.

[5] Harlow JE, Ma X, Li J, Logan E, Liu Y, Zhang N, Ma L, Glazier SL, Cormier MME, Genovese M, Buteau S, Cameron A, Stark JE, Dahn JR. A wide range of testing results on an excellent lithium-ion cell chemistry to be used as benchmarks for new battery technologies. J Electrochem Soc 2019;166(13):A3031–44. https://doi.org/10.1149/2.0981913jes.

[6] Barkholtz HM, Fresquez A, Chalamala BR, Ferreira SR. A database for comparative electrochemical performance of commercial 18650-format lithium-ion cells. J Electrochem Soc 2017;164(12):A2697. https://doi.org/10.1149/2.1701712jes.

[7] Muenzel V, Hollenkamp AF, Bhatt AI, de Hoog J, Brazil M, Thomas DA, Mareels I. A comparative testing study of commercial 18650-format lithium-ion battery cells. J Electrochem Soc 2015;162(8):A1592. https://doi.org/10.1149/2.0721508jes.

[8] Bank T, Klamor S, Löffler N, Sauer DU. Performance benchmark of state-of-the-art high-power lithium-ion cells and implications for their usability in low-voltage applications. J Energy Storage 2021;36:102383. https://doi.org/10.1016/j.est.2021.102383.

[9] Momen F, Rahman K, Son Y. Electrical propulsion system design of chevrolet bolt battery electric vehicle. IEEE Trans Ind Appl 2018;55(1):376–84. https://doi.org/10.1109/ECCE.2016.7855076.

[10] Wegener K, Andrew S, Raatz A, Dröder K, Herrmann C. Disassembly of electric vehicle batteries using the example of the audi Q5 hybrid system. Procedia CIRP 2014;23:155–60. https://doi.org/10.1016/j.procir.2014.10.098.

[11] Kovachev Schröttner, Gstrein Aiello, Hanzu Wilkening, Foitzik Wellm, Sinz Ellersdorfer. Analytical dissection of an automotive Li-ion pouch cell. Batteries 2019;5(4):67. https://doi.org/10.3390/batteries5040067.

[12] Marshall J, Gastol D, Sommerville R, Middleton B, Goodship V, Kendrick E. Disassembly of li ion cells—characterization and safety considerations of a recycling scheme. Metals 2020;10(6):773. https://doi.org/10.3390/met10060773.

[13] Löbberding H, Wessel S, Offermanns C, Kehrer M, Rother J, Heimes H, Kampker A. From cell to battery system in BEVs: analysis of system packing efficiency and cell types. World Electr. Veh. J. 2020;11(4):77. https://doi.org/10.3390/wevj11040077.

[14] Oh G, Leblanc DJ, Peng H. Vehicle energy dataset (VED), A large-scale dataset for vehicle energy consumption research. IEEE Trans Intell Transport Syst 2020:1–11. https://doi.org/10.1109/TITS.2020.3035596.

[15] Diez J. Advanced vehicle testing and evaluation, final technical report encompassing project activities from october 1, 2011 to april 30, 2018, Tech. rep. Arlington Heights, IL (United States): Intertek Testing Services, NA, Inc.; 2018.

[16] European Parliament. Regulation (EU) 2018/858 of the European Parliament and of the Council of 30 May 2018 on the approval and market surveillance of motor vehicles and their trailers, and of systems, components and separate technical units intended for such vehicles, amending Regulations (EC) No 715/2007 and (EC) No 595/2009 and repealing Directive 2007/46/EC. URL, https://eur-lex.europa.eu/eli/reg/2018/858/oj; 30.05.2018. Accessed at 24 December 2021.

[17] Merkle L, Pöthig M, Schmid F. Estimate e-golf battery state using diagnostic data and a digital twin. Batteries 2021;7(1):15. https://doi.org/10.3390/batteries7010015.

[18] Mussa AS, Klett M, Lindbergh G, Lindström RW. Effects of external pressure on the performance and ageing of single-layer lithium-ion pouch cells. J Power Sources 2018;385:18–26. https://doi.org/10.1016/j.jpowsour.2018.03.020.

[19] Wassiliadis N, Ank M, Wildfeuer L, Kick MK, Lienkamp M. Experimental investigation of the influence of electrical contact resistance on lithium-ion battery testing for fast-charge applications. Appl Energy 2021;295:117064. https://doi.org/10.1016/j.apenergy.2021.117064.

[20] Barai A, Uddin K, Dubarry M, Somerville L, McGordon A, Jennings P, Bloom I. A comparison of methodologies for the non-invasive characterisation of commercial Li-ion cells. Prog Energy Combust Sci 2019;72:1–31. https://doi.org/10.1016/j.pecs.2019.01.001.

[21] Epding B, Rumberg B, Jahnke H, Stradtmann I, Kwade A. Investigation of significant capacity recovery effects due to long rest periods during high current cyclic aging tests in automotive lithium ion cells and their influence on lifetime. J Energy Storage 2019;22:249–56. https://doi.org/10.1016/j.est.2019.02.015. URL.

[22] F. J. Günter, N. Wassiliadis, State of the art of lithium-ion pouch cells in automotive applications: cell teardown and characterization, J Electrochem Soc:https://doi.org/10.1149/1945-7111/ac4e11.

[23] Fuchss S, Michaelides A, Stocks O, Devenport R. The propulsion system of the new jaguar i-pace. MTZ worldwide 2019;80(1):18–25. https://doi.org/10.1007/s38313-018-0123-4.

[24] Sturm J, Rheinfeld A, Zilberman I, Spingler FB, Kosch S, Frie F, Jossen A. Modeling and simulation of inhomogeneities in a 18650 nickel-rich, silicon-graphite lithium-ion cell during fast charging. J Power Sources 2019;412:204–23. https://doi.org/10.1016/j.jpowsour.2018.11.043.

[25] Bloom I, Jansen AN, Abraham DP, Knuth J, Jones SA, Battaglia VS, Henriksen GL. Differential voltage analyses of high-power, lithium-ion cells. J Power Sources 2005;139(1–2):295–303. https://doi.org/10.1016/j.jpowsour.2004.07.021.

[26] Bloom I, Christophersen J, Gering K. Differential voltage analyses of high-power lithium-ion cells. J Power Sources 2005;139(1–2):304–13. https://doi.org/10.1016/j.jpowsour.2004.07.022.

[27] Volkswagen AG. Powerful and scalable: The new ID. battery system. URL, https://www.volkswagenag.com/en/news/stories/2018/10/powerful-and-scalable-the-new-id-battery-system.html; 2018. Accessed at 24 December 2021.

[28] Myung S-T, Maglia F, Park K-J, Yoon CS, Lamp P, Kim S-J, Sun Y-K. Nickel-Rich layered cathode materials for automotive lithium-ion batteries: achievements and perspectives. ACS Energy Lett 2017;2(1):196–223. https://doi.org/10.1021/acsenergylett.6b00594.

[29] Jung R, Metzger M, Maglia F, Stinner C, Gasteiger HA. Oxygen release and its

effect on the cycling stability of LiNi x Mn y Co z O 2 (NMC) cathode materials for Li-ion batteries. J Electrochem Soc 2017;164(7):A1361–77. https://doi.org/10.1149/2.0021707jes.
[30] Noh H-J, Youn S, Yoon CS, Sun Y-K. Comparison of the structural and electrochemical properties of layered Li[NixCoyMnz]O2 (x = 1/3, 0.5, 0.6, 0.7, 0.8 and 0.85) cathode material for lithium-ion batteries. J Power Sources 2013;233:121–30. https://doi.org/10.1016/j.jpowsour.2013.01.063.
[31] Dou F, Shi L, Chen G, Zhang D. Silicon/carbon composite anode materials for lithium-ion batteries. Electrochem Energy Rev 2019;2(1):149–98. https://doi.org/10.1007/s41918-018-00028-w.
[32] Zilberman I, Sturm J, Jossen A. Reversible self-discharge and calendar aging of 18650 nickel-rich, silicon-graphite lithium-ion cells. J Power Sources 2019;425:217–26. https://doi.org/10.1016/j.jpowsour.2019.03.109.
[33] Keil P, Jossen A. Calendar aging of NCA lithium-ion batteries investigated by differential voltage analysis and coulomb tracking. J Electrochem Soc 2017;164(1):A6066–74. https://doi.org/10.1149/2.0091701jes.
[34] Doerr J, Ardey N, Mendl G, Fröhlich G, Straßer R, Laudenbach T. The new full electric drivetrain of the audi e-tron. In: Liebl J, editor. Der Antrieb von morgen 2019, Proceedings. Wiesbaden: Springer Fachmedien Wiesbaden; 2019. p. 13–37. https://doi.org/10.1007/978-3-658-26056-9_2.
[35] Gallagher KG, Trask SE, Bauer C, Woehrle T, Lux SF, Tschech M, Lamp P, Polzin BJ, Ha S, Long B, Wu Q, Lu W, Dees DW, Jansen AN. Optimizing areal capacities through understanding the limitations of lithium-ion electrodes. J Electrochem Soc 2016;163(2):A138–49. https://doi.org/10.1149/2.0321602jes.
[36] Viswanathan VV, Choi D, Wang D, Xu W, Towne S, Williford RE, Zhang J-G, Liu J, Yang Z. Effect of entropy change of lithium intercalation in cathodes and anodes on Li-ion battery thermal management. J Power Sources 2010;195(11):3720–9. https://doi.org/10.1016/j.jpowsour.2009.11.103.
[37] Li Z, Zhang J, Wu B, Huang J, Nie Z, Sun Y, An F, Wu N. Examining temporal and spatial variations of internal temperature in large-format laminated battery with embedded thermocouples. J Power Sources 2013;241:536–53. https://doi.org/10.1016/j.jpowsour.2013.04.117.
[38] Storch M, Fath JP, Sieg J, Vrankovic D, Krupp C, Spier B, Riedel R. Temperature and lithium concentration gradient caused inhomogeneous plating in large-format lithium-ion cells. J Energy Storage 2021;41:102887. https://doi.org/10.1016/j.est.2021.102887.
[39] Wildfeuer L, Wassiliadis N, Reiter C, Baumann M, Lienkamp M. Experimental characterization of Li-ion battery resistance at the cell , module and pack level. In: 2019 fourteenth international conference on ecological vehicles and renewable energies (EVER); 2019. p. 1–12. https://doi.org/10.1109/EVER.2019.8813578.
[40] Mertens A, Vinke IC, Tempel H, Kungl H, de Haart LGJ, Eichel R-A, Granwehr J. Quantitative analysis of time-domain supported electrochemical impedance spectroscopy data of Li-ion batteries: reliable activation energy determination at low frequencies. J Electrochem Soc 2016;163(7):H521–7. https://doi.org/10.1149/2.0511607jes.
[41] Heubner C, Schneider M, Michaelis A. Investigation of charge transfer kinetics of li-intercalation in lifepo4. J Power Sources 2015;288:115–20. https://doi.org/10.1016/j.jpowsour.2015.04.103. URL.
[42] Schnell J, Nentwich C, Endres F, Kollenda A, Distel F, Knoche T, Reinhart G. Data mining in lithium-ion battery cell production. J Power Sources 2019;413:360–6. https://doi.org/10.1016/j.jpowsour.2018.12.062.
[43] Mohanty D, Hockaday E, Li J, Hensley DK, Daniel C, Wood DL. Effect of electrode manufacturing defects on electrochemical performance of lithium-ion batteries: cognizance of the battery failure sources. J Power Sources 2016;312:70–9. https://doi.org/10.1016/j.jpowsour.2016.02.007.
[44] Zilberman I, Schmitt J, Ludwig S, Naumann M, Jossen A. Simulation of voltage imbalance in large lithium-ion battery packs influenced by cell-to-cell variations and balancing systems. J Energy Storage 2020;32:101828. https://doi.org/10.1016/j.est.2020.101828.
[45] Liu X, Ai W, Naylor Marlow M, Patel Y, Wu B. The effect of cell-to-cell variations and thermal gradients on the performance and degradation of lithium-ion battery packs. Appl Energy 2019;248:489–99. https://doi.org/10.1016/j.apenergy.2019.04.108.
[46] Shi W, Hu X, Jin C, Jiang J, Zhang Y, Yip T. Effects of imbalanced currents on large-format lifepo 4/graphite batteries systems connected in parallel. J Power Sources 2016;313:198–204. https://doi.org/10.1016/j.jpowsour.2016.02.087.
[47] Yang N, Zhang X, Shang B, Li G. Unbalanced discharging and aging due to temperature differences among the cells in a lithium-ion battery pack with parallel combination. J Power Sources 2016;306:733–41. https://doi.org/10.1016/j.jpowsour.2015.12.079.
[48] Zilberman I, Ludwig S, Jossen A. Cell-to-cell variation of calendar aging and reversible self-discharge in 18650 nickel-rich, silicon–graphite lithium-ion cells. J Energy Storage 2019;26:100900. https://doi.org/10.1016/j.est.2019.100900.
[49] Wildfeuer L, Lienkamp M. Quantifiability of inherent cell-to-cell variations of commercial lithium-ion batteries. eTransportation; 2021, 100129. https://doi.org/10.1016/j.etran.2021.100129.
[50] An F, Chen L, Huang J, Zhang J, Li P. Rate dependence of cell-to-cell variations of lithium-ion cells. Sci Rep 2016;6:35051. https://doi.org/10.1038/srep35051.
[51] Schuster SF, Brand MJ, Berg P, Gleissenberger M, Jossen A. Lithium-ion cell-to-cell variation during battery electric vehicle operation. J Power Sources 2015;297:242–51. https://doi.org/10.1016/j.jpowsour.2015.08.001.
[52] Rumpf K, Naumann M, Jossen A. Experimental investigation of parametric cell-to-cell variation and correlation based on 1100 commercial lithium-ion cells. J Energy Storage 2017;14:224–43. https://doi.org/10.1016/j.est.2017.09.010.
[53] Barreras JV, Raj T, Howey DA, Schaltz E. Results of screening over 200 pristine lithium-ion cells. In: 2017 IEEE vehicle power and propulsion conference. VPPC; 2017. p. 1–6. https://doi.org/10.1109/VPPC.2017.8331054.
[54] Campestrini C, Keil P, Schuster SF, Jossen A. Ageing of lithium-ion battery modules with dissipative balancing compared with single-cell ageing. J Energy Storage 2016;6:142–52. https://doi.org/10.1016/j.est.2016.03.004.
[55] A. Devie, G. Baure, M. Dubarry, Intrinsic variability in the degradation of a batch of commercial 18650 lithium-ion cells, Energies 11 (5). doi:10.3390/en11051031.
[56] Zilberman I, Ludwig S, Jossen A. Cell-to-cell variation of calendar aging and reversible self-discharge in 18650 nickel-rich, silicon–graphite lithium-ion cells. J Energy Storage 2019;26:100900. https://doi.org/10.1016/j.est.2019.100900.
[57] Schindler M, Sturm J, Ludwig S, Schmitt J, Jossen A. Evolution of initial cell-to-cell variations during a three-year production cycle. eTransportation 2021;8:100102. https://doi.org/10.1016/j.etran.2020.100102.
[58] Baumann M, Wildfeuer L, Rohr S, Lienkamp M. Parameter variations within li-ion battery packs – theoretical investigations and experimental quantification. J Energy Storage 2018;18:295–307. https://doi.org/10.1016/j.est.2018.04.031.
[59] Mertens A, Vinke IC, Tempel H, Kungl H, de Haart LGJ, Eichel R-A, Granwehr J. Quantitative analysis of time-domain supported electrochemical impedance spectroscopy data of li-ion batteries: reliable activation energy determination at low frequencies. J Electrochem Soc 2016;163(7):H521–7. https://doi.org/10.1149/2.0511607jes.
[60] Pesaran AA. Battery thermal models for hybrid vehicle simulations. J Power Sources 2002;110(2):377–82. https://doi.org/10.1016/S0378-7753(02)00200-8.
[61] Chung Y, Kim MS. Thermal analysis and pack level design of battery thermal management system with liquid cooling for electric vehicles. Energy Convers Manag 2019;196:105–16. https://doi.org/10.1016/j.enconman.2019.05.083.
[62] Wang J, Lu S, Wang Y, Li C, Wang K. Effect analysis on thermal behavior enhancement of lithium–ion battery pack with different cooling structures. J Energy Storage 2020;32:101800. https://doi.org/10.1016/j.est.2020.101800.
[63] Yang X-G, Liu T, Gao Y, Ge S, Leng Y, Wang D, Wang C-Y. Asymmetric temperature modulation for extreme fast charging of lithium-ion batteries. Joule 2019;3(12):3002–19. https://doi.org/10.1016/j.joule.2019.09.021.
[64] Yin Y, Choe S-Y. Actively temperature controlled health-aware fast charging method for lithium-ion battery using nonlinear model predictive control. Appl Energy 2020;271:115232. https://doi.org/10.1016/j.apenergy.2020.115232.
[65] Liu T, Ge S, Yang X-G, Wang C-Y. Effect of thermal environments on fast charging li-ion batteries. J Power Sources 2021;511:230466. https://doi.org/10.1016/j.jpowsour.2021.230466.
[66] Preger Y, Barkholtz HM, Fresquez A, Campbell DL, Juba BW, Romàn-Kustas J, Ferreira SR, Chalamala B. Degradation of commercial lithium-ion cells as a function of chemistry and cycling conditions. J Electrochem Soc 2020;167(12):120532. https://doi.org/10.1149/1945-7111/abae37.
[67] Yuksel T, Litster S, Viswanathan V, Michalek JJ. Plug-in hybrid electric vehicle lifepo4 battery life implications of thermal management, driving conditions, and regional climate. J Power Sources 2017;338:49–64. https://doi.org/10.1016/j.jpowsour.2016.10.104.
[68] Neubauer J, Wood E. Thru-life impacts of driver aggression, climate, cabin thermal management, and battery thermal management on battery electric vehicle utility. J Power Sources 2014;259:262–75. https://doi.org/10.1016/j.jpowsour.2014.02.083.
[69] Baumhöfer T, Brühl M, Rothgang S, Sauer DU. Production caused variation in capacity aging trend and correlation to initial cell performance. J Power Sources 2014;247:332–8. https://doi.org/10.1016/j.jpowsour.2013.08.108.
[70] P. M. Attia, A. Bills, F. B. Planella, P. Dechent, G. d. Reis, M. Dubarry, P. Gasper, R. Gilchrist, S. Greenbank, D. Howey, O. Liu, E. Khoo, Y. Preger, A. Soni, S. Sripad, A. G. Stefanopoulou, V. Sulzer, Knees in lithium-ion battery aging trajectories. https://doi.org/10.48550/arXiv.2201.02891.
[71] Ecker M, Nieto N, Käbitz S, Schmalstieg J, Blanke H, Warnecke A, Sauer DU. Calendar and cycle life study of Li(NiMnCo)O2-based 18650 lithium-ion batteries. J Power Sources 2014;248:839–51. https://doi.org/10.1016/j.jpowsour.2013.09.143.
[72] Maheshwari A, Heck M, Santarelli M. Cycle aging studies of lithium nickel manganese cobalt oxide-based batteries using electrochemical impedance spectroscopy. Electrochim Acta 2018;273:335–48. https://doi.org/10.1016/j.electacta.2018.04.045.
[73] Paul N, Keil J, Kindermann FM, Schebesta S, Dolotko O, Mühlbauer MJ, Kraft L, Erhard SV, Jossen A, Gilles R. Aging in 18650-type Li-ion cells examined with neutron diffraction, electrochemical analysis and physico-chemical modeling. J Energy Storage 2018;17:383–94. https://doi.org/10.1016/j.est.2018.03.016.
[74] Schmalstieg J, Käbitz S, Ecker M, Sauer DU. A holistic aging model for Li(NiMnCo)O2 based 18650 lithium-ion batteries. J Power Sources 2014;257:325–34. https://doi.org/10.1016/j.jpowsour.2014.02.012.
[75] Naumann M, Spingler FB, Jossen A. Analysis and modeling of cycle aging of a commercial LiFePO4/graphite cell. J Power Sources 2020;451:227666. https://doi.org/10.1016/j.jpowsour.2019.227666.